

## Reverse Engineering the Locomotion of a Stem Amniote

John A. Nyakatura<sup>\*,1,2</sup>, Kamilo Melo<sup>+3</sup>, Tomislav Horvat<sup>+3</sup>, Kostas Karakasiliotis<sup>3</sup>, Vivian R. Allen<sup>4</sup>, Amir Andikfar<sup>5</sup>, Emanuel Andrada<sup>6</sup>, Patrick Arnold<sup>6</sup>, Jonas Lauströer<sup>5,7</sup>, John R. Hutchinson<sup>4</sup>, Martin S. Fischer<sup>6</sup> and Auke J. Ijspeert<sup>3</sup>.

\*: Corresponding author

+: These authors contributed equally

<sup>1</sup>: AG Morphologie und Formengeschichte, Institut für Biologie, Humboldt Universität zu Berlin, Berlin, Germany.

<sup>2</sup>: Bild Wissen Gestaltung. Ein interdisziplinäres Labor, Humboldt Universität zu Berlin, Berlin, Germany.

<sup>3</sup>: Biorobotics Laboratory, École Polytechnique Fédérale de Lausanne (EPFL), Lausanne, Switzerland.

<sup>4</sup>: Structure & Motion Laboratory, Department of Comparative Biomedical Sciences, The Royal Veterinary College, North Mymms, UK.

<sup>5</sup>: Fakultät Design, Medien und Information, Department Design, Hochschule für Angewandte Wissenschaften, Hamburg, Germany.

<sup>6</sup>: Institut für Zoologie und Evolutionsforschung mit Phyletischem Museum, Ernst-Haeckel-Haus und Biologiedidaktik, Friedrich-Schiller-Universität Jena, Jena, Germany

<sup>7</sup>: Knowledge Visualisation, Zürcher Hochschule der Künste, Zurich, Switzerland.

Reconstructing the locomotion of extinct vertebrates offers insight into their paleobiology and helps to conceptualize major transitions in vertebrate evolution<sup>1,2,3,4</sup>. Estimation of a fossil's locomotor behaviour, however, remains problematic because of limited information preserved and lack of direct correspondence between form and function<sup>5,6</sup>. The evolution of advanced; i.e. more erect, balanced and mechanical power-saving; locomotion on land was previously linked to the terrestrialization and diversification of amniote lineages<sup>7</sup>. No quantitative reconstructions of locomotor characteristics of stem amniote fossils have been attempted. Generally, methods suffer from over-reliance on anatomical features alone, ambiguous locomotor information preserved in ichnofossils, or unspecific modelling of locomotor dynamics. Here we quantitatively examine plausible gaits of the stem amniote *Orobates pabsti*, a species known from a complete body fossil preserved in association with trackways<sup>8</sup>. We reconstruct likely gaits matching the footprints, and ask whether *Orobates* already exhibited locomotor characteristics that were previously linked to crown amniote diversification. Our integrative methodology uses constraints from biomechanically relevant metrics that also apply to extant tetrapods. The framework uses *in vivo* assessment of locomotor mechanics in four extant species to guide an anatomically informed kinematic simulation of *Orobates* as well as dynamic simulations and biorobotics to filter the parameter space for plausible gaits. The approach was validated with two extant species with different morphologies, gaits and footprints. Our metrics indicate that *Orobates* exhibited more advanced locomotion than assumed for earlier tetrapods<sup>7,9</sup>, suggesting advanced terrestrial locomotion preceded the diversification of crown amniotes. Readers can interactively explore filters constraining our simulations on an accompanying interactive website and revise our approach with new data, assumptions or methods.

Reconstructing the locomotion of key vertebrate fossils is critical for inferring major transitions in vertebrate evolution. Solely analyzing the anatomy of fossils suffers from joint ranges of motion much larger than those used during locomotion and redundancy (excess degrees of freedom) in appendages<sup>10,11,12</sup>. Additionally, such studies often neglect the biomechanics of the whole organism (e.g., energetics and centre of mass mechanics<sup>13</sup>). Analyses of extant species demonstrate that diverse anatomical conditions can potentially enable similar function, questioning a direct correspondence between form and function<sup>5,11</sup>. In contrast, reconstructions relying entirely on mechanical modelling and engineering are limited, because they often neglect anatomical detail. Finally, reconstructions relying solely on interpretation of fossil trackways suffer from uncertainty of different movements or gaits that produce nearly identical trackways<sup>14</sup>. Here we propose an integrative approach that makes use of the advantages of these different strategies to reconstruct locomotion of tetrapod fossils, focusing on inferring the potential gaits of the stem amniote *Orobates pabsti*,

a basal diadectid from the Permian (Fig. 1)<sup>15</sup>. Based on prior qualitative assessment it was hypothesized that *Orobates* may have been capable of “increased speed, greater maneuverability, and more efficient support” than earlier tetrapods<sup>16</sup>.

A three-dimensional skeletal reconstruction of *Orobates* [17] was used to design three types of models: a kinematic *Orobates* simulation, the physical OroBOT robot, and the dynamic OroBOT simulation (Fig. 1, Extended Data 1a-f). A fossil trackway assigned to *Orobates*<sup>8</sup> (Extended Data 1g) was idealized and used as a hard constraint in the kinematic simulation and as a metric in the dynamic simulation (Extended Data 1h-k). The kinematic *Orobates* simulation was used to identify anatomically plausible kinematic parameter combinations. The dynamic OroBOT simulation aimed to quantify the physics of locomotion, assessing mechanical power expenditure, the ability to walk without excessive tilting, ground reaction forces (GRF) similar to the studied extant species, and the precision of matching the fossil trackway. The physical OroBOT was used to validate the results of the dynamic simulation under real-world conditions. We systematically characterized possible sprawling gaits (of *Orobates*, extant animals, and our simulations) in a “sprawling gait space” (SGS) based on body height, lateral bending of the vertebral column, and long-axis rotation (LAR) and retraction in the proximal limb joints (shoulder and hip). These quantities are the most important contributors to progression during sprawling tetrapod locomotion (Extended Data 2)<sup>18,19</sup>.

The locomotor mechanics and track-making of salamanders, skinks, iguanas, and caimans were analyzed and located in the SGS. Extant species sampling encompassed the phylogenetic bracket of the an-amniote to amniote transition<sup>20,21</sup>. Species had desirable traits such as usually exhibiting sprawling locomotion, different ecologies and diverse gross morphologies such as different ratios of limb length to snout-vent length (Extended Data 3a). Our sampling thus covered a reasonable portion of the mechanical disparity exhibited in tetrapods using quadrupedal sprawling locomotion. It was not our goal to find an analogue for *Orobates*. Instead, we aimed to identify principles of sprawling tetrapod locomotion that apply to most, if not all, sprawling taxa, and use these to infer the most-likely gaits of *Orobates*.

Comparative x-ray motion analysis with simultaneous GRF measurement (Fig. 2a-d) revealed that salamanders and skinks (both limbs) as well as iguanas (hindlimbs) exhibited relatively less body height (i.e., hyper-sprawled posture), while more erect limb postures were observed in caimans (both limbs) and iguanas (forelimbs) (Fig. 2e). Humeral and femoral LAR was inversely related to humeral and femoral retraction ( $P < 0.001$  in MLR analysis) (Fig. 2f,g). To facilitate 3D viewing, we therefore show data for LAR to the

exclusion of retraction data in the SGS. Moreover, humeral and femoral LAR were inversely related to body height ( $P = 0.045$  for forelimbs,  $P < 0.001$  for hindlimbs); i.e., more erect limbs exhibited less humeral and femoral LAR. An increase in body height also resulted in increased humeral retraction ( $P < 0.001$ ). Increased spine bending resulted in decreased femoral retraction ( $P < 0.001$ ) and was positively related to body height ( $P < 0.001$ ) (Fig. 2h). Despite differences in the kinematic patterns between the hyper-sprawled and more erect limbs, the timing of peak vertical GRF during sprawling locomotion remained similar. Forelimb vertical GRF patterns (Fig. 2i) were similar in our sample of extant species, with a peak force of  $\sim 0.5$  body weight units (BWU;  $0.46 \pm 0.02$ ) and occurrence of peak force at  $\sim 2/3$  of contact time ( $61.3\% \pm 4.8\%$ ), indicating maintenance of dynamic similarity in these aspects. Hindlimb vertical GRF profiles (Fig. 2j) were less homogeneous (peak force:  $0.37 \pm 0.17$  BWU), but had a similar timing of peak force at  $\sim 1/3$  of contact time ( $31.3\% \pm 6.3\%$ ). Trackway parameters of *Orobates* (blue in Fig. 2k-m) were intermediate to extant species. Given these principles of sprawling locomotion in extant species, some similarities (e.g., in the forelimb GRF pattern) can be inferred for the fossil.

In light of the extant animal data, we linked both simulations (kinematic *Orobates* and dynamic OroBOT) by focussing on body height, spine bending, and LAR of the humerus and femur, and visualising these in SGS plots (Fig. 3a-c) to systematically vary these parameters, resulting in different gaits. Using the digital marionette of *Orobates*, we varied all kinematic parameters from “none” to “exaggerated” to cover a larger parameter space than covered by the extant species and evaluated each gait for anatomical plausibility. To rule out anatomically implausible solutions in the kinematic *Orobates* simulation,  $n=200$  permutations of parameter combinations ( $n=100$  for forelimbs and hindlimbs each) were evaluated based on the occurrence of bone collisions in the proximal limb joints and disarticulations of the wrist or ankle during a limb’s ground contact (Extended Data 2). For each bone, collisions were scored in four levels with a maximum score for perfect plausibility (no joint disarticulations and/or bone collisions). A combined score for both limb pairs (eight levels in total) created a region of anatomically plausible kinematic parameter combinations within the SGS with little to moderate humeral and femoral LAR (and hence pronounced retraction), intermediate to high body height, and moderate lateral spine bending (Fig. 3c).

Assessment of anatomical plausibility (kinematic metric) was complemented by dynamic OroBOT simulation, to further constrain the solution space (dynamic metrics). OroBOT was designed to closely mimic the fossil’s anatomy, mass distribution of body segments, and position of centre of mass (Extended Data 1a-c and 4a-c). Dynamic simulation was used to systematically test  $n=512$  ( $8 \times 8 \times 8$ ) combinations of kinematic parameters analogous to the kinematic simulation. Four biologically meaningful dynamic metrics were designed to

exclude unlikely gaits from the SGS and to identify dynamically plausible gaits (Supplementary Information 1,2): 1) Power expenditure, measured as the reciprocal of positive torque times velocity summed over the 28 actuated joints for one stride of OroBOT. Gaits that required little power received a high score. Animals are hypothesized to choose gaits that minimize power expenditure to produce torque about their joints<sup>12</sup>. 2) Balance, quantified as the reciprocal of the body's roll and pitch rate. Animals are hypothesized to minimize rapid tilting of the body to not compromise optical and vestibular perception<sup>22</sup>. High scores in balance correspond to gaits that have low rates of tilting. 3) Precision, measured as the accuracy of the robot's foot placement within the fossil trackways. 4) Similarity of GRFs to extant species, here evaluated by measuring the similarity of the simulated robot's forelimb vertical GRF component to the homogeneous forelimb vertical GRF component averaged across the extant species.

For validation, we applied our simulation approach to an extant caiman (Extended Data 5) and a salamander (Extended Data 6). Similarly to *Orobates*, we tried to identify their most likely gaits in their respective SGS given only their skeletal anatomy and their trackways (Methods). Demonstrating the reliability of the approach, the predicted gaits were found to be nested within the respective animal data in their SGS, in particular with erect gaits in the caiman and low body height gaits in the salamander.

To identify plausible gaits of *Orobates*, we excluded low-ranked solutions for each metric (see accompanying interactive website and Methods)<sup>11</sup>. Here we present an exemplar analysis with all dynamic metrics having a cut-off threshold set to 50%, which filtered the 50% lowest-ranked solutions of each metric from the dynamic simulation. Results from the four individual dynamic metrics were then combined to create a dynamic score (more plausible gaits). The final step to arrive at plausible gait solutions for *Orobates* combined these dynamically plausible gaits with the anatomically plausible gaits (kinematic metric). With the suggested exclusion settings, the overall SGS was narrowed down to one region of parameter combinations that achieved the highest score (Fig. 3d). These plausible solutions were gaits with moderate LAR (25-46°) and spine bending (17-35°) combined with considerable body height (0.44 [percent of inter-girdle distance]). They may not be the only parameter combinations yielding the maximum high score, depending on the cut-off thresholds of the individual metrics, but are representative of a region within the SGS with a clustering of gait solutions indicative of more erect (adducted) limb posture. The plausible *Orobates* gaits were located close to the caiman gaits in the SGS (Fig. 3d). As further validation of our results, we compared dimensionless joint torque around the shoulder at peak vertical forelimb GRF and found OroBOT (0.51; read out from the simulated servo motors; Extended Data 7) to exhibit similar values as extant tetrapods (0.43 ± 0.07).

The physical OroBOT model is a robotic system whose design and control was based on a previous biomimetic platform which successfully replicated kinematics and dynamics of a walking salamander, but here matching the *Orobates* morphology (Supplementary Information 3-11 and Methods)<sup>23</sup>. Independent of their score in the SGS, 15 different gaits were tested in OroBOT, closely matching the dynamic simulation in terms of forward speed, body orientation over time, and foot steps (see accompanying interactive website and Supplementary Video 14). Using gaits suggested by the aforementioned exclusion settings, the physical robot was capable of reproducing trackway parameters associated with *Orobates* (Fig. 3e and Supplementary Video 14).

Quantitative reconstruction of *Orobates*'s locomotion is consistent with previous qualitative locomotor postulations based on fossil trackways<sup>8,16</sup> and was found here to be relatively erect (within the spectrum of sprawling locomotion), balanced and mechanically power-saving. More erect limb postures are linked with greater capacity for speed<sup>24</sup>, reduced torsional stresses occurring at limb long bone midshafts<sup>1,25,26</sup>, and reduced power usage to accelerate the body in the direction of travel<sup>27</sup>. *Orobates*'s locomotion was advanced (according to the metrics studied here) in comparison to earlier tetrapods<sup>9</sup>. Contrasting with previous suggestions<sup>7</sup>, the presence of these advanced terrestrial locomotor properties may be assumed in the last common ancestor of diadectids and amniotes; i.e. within the amniote stem lineage and preceding the subsequent rapid radiation of crown amniotes. Future studies may critically re-evaluate and expand the proposed metrics here and refine our results. Similar integrative approaches may be adopted for comparable research questions concerning major transitions in vertebrate evolution such as the origin of bipedality or active flight using quantitative metrics based on empirical data and/or validated simulations to exclude unlikely locomotor reconstructions while accounting for uncertainty<sup>11</sup>.

## References

- 1: Blob, R. W. (2001). Evolution of hindlimb posture in nonmammalian therapsids: biomechanical tests of paleontological hypotheses. *Paleobiology*, 27(1), 14-38.
- 2: McInroe, B., Astley, H. C., Gong, C., Kawano, S. M., Schiebel, P. E., Rieser, J. M., ... & Goldman, D. I. (2016). Tail use improves performance on soft substrates in models of early vertebrate land locomotors. *Science*, 353(6295), 154-158.
- 3: Gingerich, P. D. (2003). Land-to-sea transition in early whales: evolution of Eocene Archaeoceti (Cetacea) in relation to skeletal proportions and locomotion of living semiaquatic mammals. *Paleobiology*, 29(3), 429-454.
- 4: Pierce, S. E., Clack, J. A., & Hutchinson, J. R. (2012). Three-dimensional limb joint mobility in the early tetrapod Ichthyostega. *Nature*, 486(7404), 523.
- 5: Lauder, G. V. (1995). On the inference of function from structure. *Functional morphology in vertebrate paleontology*, 1-18.

- 6: Losos, J. B. (2011). Convergence, adaptation, and constraint. *Evolution*, 65(7), 1827-1840.
- 7: Sumida, S. S., & Modesto, S. (2001). A phylogenetic perspective on locomotory strategies in early amniotes. *American Zoologist*, 41(3), 586-597.
- 8: Voigt, S., Berman, D. S., & Henrici, A. C. (2007). First well-established track-trackmaker association of Paleozoic tetrapods based on *Ichniotherium* trackways and diadectid skeletons from the Lower Permian of Germany. *Journal of Vertebrate Paleontology*, 27(3), 553-570.
- 9: Kawano, S. M., & Blob, R. W. (2013). Propulsive forces of mudskipper fins and salamander limbs during terrestrial locomotion: implications for the invasion of land. *Integrative and comparative biology*, 53(2), 283-294.
- 10: Nicolas, G., Multon, F., Berillon, G., & Marchal, F. (2007). From bone to plausible bipedal locomotion using inverse kinematics. *Journal of biomechanics*, 40(5), 1048-1057.
- 11: Gatesy, S. M., Bäker, M., & Hutchinson, J. R. (2009). Constraint-based exclusion of limb poses for reconstructing theropod dinosaur locomotion. *Journal of Vertebrate Paleontology*, 29(2), 535-544.
- 12: Full, R. J., & Koditschek, D. E. (1999). Templates and anchors: neuromechanical hypotheses of legged locomotion on land. *Journal of experimental biology*, 202(23), 3325-3332.
- 13: Sellers, W. I., Manning, P. L., Lyson, T., Stevens, K., & Margetts, L. (2009). Virtual palaeontology: gait reconstruction of extinct vertebrates using high performance computing. *Palaeontologia Electronica*, 12(3), 11A.
- 14: Stevens, K. A., Ernst, S., & Marty, D. (2016). Uncertainty and ambiguity in the interpretation of sauropod trackways. *Dinosaur tracks—The next steps*, 227-243.
- 15: Berman, D. S., Henrici, A. C., Kissel, R. A., Sumida, S. S., & Martens, T. (2004). A new diadectid (Diadectomorpha), *Orobates pabsti*, from the Early Permian of central Germany. *Bulletin of Carnegie Museum of Natural History*, 1-36.
- 16: Berman, D. S., & Henrici, A. C. (2003). Homology of the astragalus and structure and function of the tarsus of Diadectidae. *Journal of Paleontology*, 77(1), 172-188.
- 17: Nyakatura, J. A., Allen, V. R., Lauströer, J., Andikfar, A., Danczak, M., Ullrich, H. J., ... & Fischer, M. S. (2015). A three-dimensional skeletal reconstruction of the stem amniote *Orobates pabsti* (Diadectidae): analyses of body mass, centre of mass position, and joint mobility. *PloS one*, 10(9), e0137284.
- 18: Edwards, J. L. (1977). The evolution of terrestrial locomotion. In *Major patterns in vertebrate evolution* (pp. 553-577). Springer, Boston, MA.
- 19: Ashley-Ross, M. (1994). Hindlimb kinematics during terrestrial locomotion in a salamander (*Dicamptodon tenebrosus*). *Journal of experimental biology*, 193(1), 255-283.
- 20: Witmer, L. M. (1995). The extant phylogenetic bracket and the importance of reconstructing soft tissues in fossils. *Functional morphology in vertebrate paleontology*, 1, 19-33.

- 21: Laurin, M., & Reisz, R. R. (1995). A reevaluation of early amniote phylogeny. *Zoological Journal of the Linnean Society*, 113(2), 165-223.
- 22: Dunbar, D. C., Macpherson, J. M., Simmons, R. W., & Zarcades, A. (2008). Stabilization and mobility of the head, neck and trunk in horses during overground locomotion: comparisons with humans and other primates. *Journal of Experimental Biology*, 211(24), 3889-3907.
- 23: Karakasiliotis, K., Thandiackal, R., Melo, K., Horvat, T., Mahabadi, N. K., Tsitkov, S., ... & Ijspeert, A. J. (2016). From cineradiography to biorobots: an approach for designing robots to emulate and study animal locomotion. *Journal of The Royal Society Interface*, 13(119), 20151089.
- 24: Fuller, P. O., Higham, T. E., & Clark, A. J. (2011). Posture, speed, and habitat structure: three-dimensional hindlimb kinematics of two species of padless geckos. *Zoology*, 114(2), 104-112.
- 25: Reilly, S. M., Willey, J. S., Biknevicius, A. R., & Blob, R. W. (2005). Hindlimb function in the alligator: integrating movements, motor patterns, ground reaction forces and bone strain of terrestrial locomotion. *Journal of Experimental Biology*, 208(6), 993-1009.
- 26: Blob, R. W., & Biewener, A. A. (2001). Mechanics of limb bone loading during terrestrial locomotion in the green iguana (*Iguana iguana*) and American alligator (*Alligator mississippiensis*). *Journal of Experimental Biology*, 204(6), 1099-1122.
- 27: Riskin, D. K., Kendall, C. J., & Hermanson, J. W. (2016). The crouching of the shrew: Mechanical consequences of limb posture in small mammals. *PeerJ*, 4, e2131.

## **Acknowledgments**

We thank R. Petersohn, I. Weiß, S. Curth, B. Weißflog, J. Stampe, R. Häfner, U. Feiler-Kress, O. Demuth, S. Clemens, T. Blochberger, and M. Krüger for support during data acquisition and analysis of extant animals. We further thank N. Schilling, T. Martens, A. Henrici, S. Sumida, and D. Berman for input during the conceptualisation and feedback at various stages of the project. The project received funding from the Volkswagen Foundation (AZ 90222 to JAN and MSF) and the Daimler and Benz Foundation (32-08/12 to JAN). JAN was also supported by the German Research Council (DFG EXC 1027). TH and KM were supported by the Swiss National Science Foundation through the NCCR Robotics. JRH was supported by the UK Natural Environment Research Council (NE/K004751/1).

## **Author contributions**

JAN, KK, KM, JRH, MSF, AJI conceived the study. JAN, EA, VA, JRH performed the extant animal motion analysis. JAN, PA, AA, JL performed the digital reconstruction of the fossil. JAN, AA, JL performed the kinematic simulation. TH, KM performed the dynamic simulation. KM analyzed the scaling and dynamic similarity. KK, KM designed and built the robot. TH,

KM designed and carried out the experiments with the robot. KM, TH designed, and TH implemented the interactive website. JAN, KM, TH wrote the manuscript. All authors contributed to and approved the final draft of the manuscript.

### **Data availability statement**

*Orobates* gait solutions can be explored on the interactive website: ([https://biorob2.epfl.ch/pages/Orobates\\_interactive/](https://biorob2.epfl.ch/pages/Orobates_interactive/)). See (Supplementary Video 15) for help using the website. Data for Fig. 2 and Extended Data 5, 6, are provided in Supplementary Data 12, 13, respectively. X-ray videos are available from the Jena Collection of X-Ray Movies database (<https://szeb.thulb.uni-jena.de>) upon request. The digital marionette of *Orobates* is available from the corresponding author upon reasonable request. Webots and Matlab code can be found in the GIT repository ([https://gitlab.com/thorvat27/orobot\\_dynamic\\_simulation](https://gitlab.com/thorvat27/orobot_dynamic_simulation)).

## Figure legends

Fig. 1: **Flow chart of the basic steps of analysis.** **Data acquisition:** digitizing holotype specimen of *Orobates* and fossil trackways; conducting x-ray motion analysis and measuring ground reaction forces of extant animals. **Simulation:** kinematic simulation of a digital marionette of *Orobates*; dynamic simulation of OroBOT; using constraints (anatomy of the holotype specimen, *Orobates*'s trackway parameters, mechanical principles of sprawling locomotion of extant animals). **Gait solutions:** Combining kinematic and dynamic filters to exclude unlikely gaits, narrow down the parameter space and compare it with animal data. **Robotics:** Demonstrating validity of gait solutions. Cut-off thresholds given to filters can be manipulated and representative videos of the animals, all simulated permutations of the dynamic OroBOT, and the kinematic *Orobates* simulations can be explored using the interactive website accompanying this paper ([https://biorob2.epfl.ch/pages/Orobates\\_interactive/](https://biorob2.epfl.ch/pages/Orobates_interactive/)).

Fig. 2: **Extant animal data.** Subjects chose their preferred gait and speed and exhibited walking trots and lateral sequence gaits (limb phase (LP):  $0.43 \pm 0.06$  (mean  $\pm$  standard deviation); duty factor (D):  $0.67 \pm 0.1$ ; stride frequency:  $0.75 \pm 0.4$ ). **(a-d)** Screenshots of x-ray motion analysis from lateral (left row) and ventro-dorsal (right row) projections. Colour code applies to all other plots (blue represents available data for *Orobates*). Data are normalized to inter-girdle distance (IGD) or body weight units (BWU) to allow comparison. **(e-h)** Comparison of mean data (ranges from min to max values during stance phase) for kinematic aspects of sprawling locomotion for shoulder girdle (SG) and forelimb (FL; salamander, skink: each  $n = 20$ ; iguana:  $n = 12$ ; caiman:  $n = 8$ ) or pelvic girdle (PG) and hindlimb (HL; salamander, skink, iguana: each  $n = 20$ ; caiman:  $n = 8$ ) (Supplementary Data 12). **(i,j)** vertical ground reaction force (GRF) profiles. **(k-m)** comparison of mean trackway data (salamander, skink, iguana: each  $n = 100$ ; caiman:  $n = 34$ ) plotted together with available data for *Orobates* trackways ( $n = 9$ ). Boxplots depict 1<sup>st</sup> and 4<sup>th</sup> quartiles as whiskers, 2<sup>nd</sup> and 3<sup>rd</sup> quartiles within box divided by median, white cross depicts mean, circles and asterisks depict outliers and extreme outliers.

Fig. 3: **Identifying plausible OroBOT gaits.** **(a)** Individual dynamic metric scores in the sprawling gait space (SGS). **(b)** Binary threshold (50th percentile) applied to the individual scores. **(c)** Shoulder and hip bone collision scores comprise the kinematic metric. **(d)** Summed scores of (b). The points whose nearest neighbour in (c) (for fore- and hind limbs each) has a score lower than the maximum (4) are excluded (transparent), providing a region of most plausible gaits (the interactive website can be used to give different weights to individual filters). Ellipsoids depict extant animal hind limb data (mean  $\pm$  standard deviation). Number of samples for each ellipsoid are the same as in Fig 2. **(e)** Snapshots of a gait within the plausible region. Axes labels in (a-c) are the same as in (d).

## Figure legends Extended Data

Extended Data 1: **Fossil, robot, and trackway detailed description (10x10 cm grid).** **(a)** *Orobates* fossil 3D views. Position of centre of mass<sup>17</sup> and lengths of different segments including inter-girdle distance (IGD) in red bar. **(b)** Scaled (1.6:1) robotic reconstruction of *Orobates* fossil called OroBOT. 3D views, position of centre of mass, segment lengths and scaled IGD in red bar. Details of head secondary scale for housing the processing unit volume. **(c)** Mass and length distributions and comparison between different segments of fossil used for the robot design. Fossil masses and lengths percentages matching in the robotic replica (Extended Data 4a-c). **(d)** Isometric view of OroBOT robot specifying the joints location. Active joints (28 in total) in red and passive joints in blue. **(e)** Passive compliant hind foot pattern (scaled 2:1), comparison with footprints from fossil tracks, and physical implementation in the robot. **(f)** Detail of the passive compliant foot with stiffness values for each of the bending axes. **(g)** Original *Orobates* - associated trackway (MNG 1840), not showing any signs of slipping or tail use during locomotion. **(h)** Detail of stride lengths, **(i)** stride widths, and **(j)** pace measurements for front, hind, left and right feet in (g). **(k)** Idealized trackway for OroBOT (Extended Data 2f). Stride length, stride width and pace (i.e., the angle between three consecutive imprints of alternate feet) correspond to averaged values of the data in (h), (i), and (j) n=18 in each case.

Extended Data 2: **Kinematic simulation of *Orobates*.** **(a-c)** The generation of body propulsion during sprawling tetrapod locomotion (exemplified for a forelimb). **(a)** The humerus (dark green) is retracted in the shoulder joint. **(b)** The humerus is rotated about its long-axis in the shoulder joint. Both mechanisms also apply to the hind limb (femoral movement relative to the hip). **(c)** Spine bending during the swing phase contributes to step length. **(d)** Fully "rigged" version of the digital *Orobates* reconstruction allowing for systematic variation of body height, LAR and retraction in the shoulders and hips, and spine bending. **(e)** Digitization and idealization of trackways (MNG 1840) for kinematic simulation. Manus (hand) and pes (foot) imprints were idealized and superimposed to fossil trackways to retain stride length, stride width, pace angulation, and manus and pes rotation. **(f)** Enlarged portion of the idealized trackway with digital reconstruction of the *Orobates pabsti* holotype specimen placed into the trackway. **(g-i)** Systematic exploration of the kinematic parameter space. Plausibility of a parameter combination was ruled out if it resulted in bone collision within the spine or within the shoulder and hip joints as well as when disarticulation of limb joints occurred (see white arrowhead in **(g)**). **(g)** Body height. **(h)** Spine bending. **(i)** Long axis rotation (LAR).

Extended Data 3: **Extant animal data.**

Table **(a)**: Experimental subjects analyzed. TL: total length; IGD: inter-girdle distance (gleno-acetabular distance). \*For comparison, data for the holotype specimen of *Orobates pabsti* measured using the digital reconstruction of the holotype specimen are provide<sup>18</sup>.

Table **(b)**: Gait parameters and calculated Froude Numbers of different sprawling posture species. (a) Spectacled caiman (*Caiman crocodilus*). (b) Green iguana (*Iguana iguana*). (c) Blue-tongued skink (*Tiliqua scincoides*). (d) Mexican salamander (*Ambystoma mexicanum*). (e) Averaged data for salamander (*Pleurodeles waltl*)<sup>23</sup>. (f) Forelimb and (g) hindlimb of Leopard gecko (*Eublepharis macularius*)<sup>45</sup>. (h) Low speed sprawling posture, (i) high speed sprawling posture, (j) low speed high walk posture and (k) high speed high walk posture of alligator (*Alligator mississippiensis*)<sup>46</sup>. Savannah monitor lizards (*Varanus exanthematicus*)<sup>47</sup>. (l) lizard 1, (m) lizard 2, (n) lizard 3, and (o) lizard 4. (p) Forelimb and (q) hindlimb of Leopard gecko (*Eublepharis macularius*)<sup>48</sup>. (r) Male and (s) female Blue-tongued skink in a previous treadmill study (*Tiliqua scincoides*)<sup>37</sup>. Colors indicate the same source of information. The Froude number was calculated as  $Fr=h(f)^2g^{-1}$ , where h is the stride length, f is the gait frequency and g gravity ( $9.81 \text{ ms}^{-2}$ ).

Extended data 4: **Fossil/Robot mass distribution (Tables a and b) and dimensions (Table c).**

Table **(a)**: Fossil/robot mass distribution. We used data for *Orobates*<sup>17</sup>. We averaged max and min plausible values of the mass of different body segments and calculate their ratios against the total body mass (also reported in Extended Data 1c). Same procedure was done for OroBOT. Differences between the mass ratios are calculated.

Table **(b)**: OroBOT mass breakdown. Mass segments correspond to a 3D printed structural part with their associated servo motors. This is the case for neck, spine and tail segments. Similarly, the head segment contains also the mass of the robot's computer and other electronic peripherals (i.e power regulator, communication, Bluetooth and Wi-fi modules). In the case of the limbs, they are composed by individual servo motors, attached to each other by small 3D printed plastic light parts i.e. Humerus/Femur, aluminum parts i.e. Antebrachium/Crus, and their corresponding plastic feet. *Orobates* had a clear difference between front and hind limb mass. Which is noticeable also by the cross sectional areas of the Humerus/Femur. This difference was hard to replicate with the materials and dimensions used in the robotic reconstruction (i.e. similar fabrication and mass for front and hind limbs). Consequently, the mass of the first and second shoulder servo motors in the forelimbs were associated with the front girdle mass, and considered as part of the trunk. In the case of the hindlimbs, only the first shoulder servo motor was considered part of the hind girdle, hence part of the trunk as well.

Table **(c)**: Length comparison between different body segments in *Orobates* and OroBOT. Organized by columns: (i) *Orobates* dimensions. (ii) *Orobates* with an initial head scale of 1.4:1 (Extended Data 1a). (iii) *Orobates* with a body scale of 1.6:1 (no head additional scaling) (Extended Data 1b). (iv) Final desired lengths of *Orobates* head and body scaled. (v) Segments to body length ratios (Extended Data 1c). (vi) Final OroBOT dimensions. (vii) OroBOT segments to body length ratios (Extended Data 1c). (viii) Mass distribution ratio differences between scaled *Orobates* and OroBOT. Data for *Orobates* taken from<sup>17</sup>. Trunk consisted of pectoral girdle, spine segments and pelvic girdle. Girdles and spine segments are depicted in light green. CoM of OroBOT was calculated using the CAD files in Autodesk Inventor® 2017 and confirmed by manual measurements.

Extended Data 5: **Kinematic simulation workflow validation using caiman.** (a): Maya screenshot of caiman digital marionette walking within digitized caiman trackways (see Methods). (b): n=100 hindlimb parameter combinations of body height, spine bending, and LAR were tested (in the same way as described for *Orobates* kinematic simulation). Scores for each combination were coded by size of the dots (largest dots assigned to perfect plausibility) and colour (dark blue assigned to perfect plausibility). Green ellipsoid depicts mean measured kinematics of caiman hindlimb from the x-ray motion analysis  $\pm$  standard deviation (n=8; green lines project the means of x, y, z onto the plane to improve readability). Note that body height less than 0.4 resulted in the body moving through the ground and spine bending over 60° resulted in bone collisions within the spine. Actual caiman kinematics (green ellipsoid) are nested within the domain identified as anatomically plausible (dark blue points), demonstrating the validity of the kinematic simulation workflow.

Extended Data 6: **Validation of the dynamic simulation workflow with *Pleurodeles*/Pleurobot.** (a) Construction of *Pleurodeles* "trackways" from a top-view x-ray video. (b) Pleurobot - a salamander-like robot used to reconstruct the salamander *Pleurodeles* gait<sup>23</sup>. Details of selection of gait parameters as in Extended Data 8. (c) Individual metric scores with the binary threshold set to 50 (50th percentile). With such exclusion, all the metrics predict a region containing the *Pleurodeles* gait (in red) n=2 for body height ( $0.23 \pm 0.01$  IGD), n=21 for

spine bending ( $(50.29 \pm 7.96)/2$  deg) and LAR ( $43.46 \pm 9.55$  deg) (Supplementary Data 13). Note in particular the low body height (around 0.2) compared to caiman (around 0.5, Extended Data 5). (d) Summed scores of the 4 dynamic metrics (power expenditure, balance, precision and GRF) in the hindlimb space with the binary threshold set to 50. (e) Exploration of Pleurobot's optimal foot stiffness and trajectory offset values (as in Extended Data 9) for the walking frequency of 0.25Hz (found by dynamic similarity analysis as in<sup>23</sup>).

Extended Data 7: **Vertical ground reaction force profile of simulated OroBOT's forelimbs**. The force profiles of gaits that scored low (5th percentile score), average (50th percentile) and high (95th percentile) in the GRF metric are shown and compared to the averaged force profile observed in the extant species ( $n=38$  trials). The gray area shows the area within which the force profiles of all  $n=512$  simulated gaits are located. The high force values of some gaits at the beginning of a stance phase are the result of foot-ground impacts while transitioning from swing to stance phase.

Extended Data 8: **OroBOT's reference frame and kinematic gait parameters**. The foot trajectory, composed of a stance phase ( $\vartheta_1 \rightarrow \vartheta_2$ ) and a swing phase ( $\vartheta_2 \rightarrow \vartheta_3 \rightarrow \vartheta_1$ ), was defined in the reference frame of the corresponding girdle. The spine motion was determined by rotation of the girdles about their vertical axis.

Extended Data 9: **Exploration of the optimal foot stiffness and trajectory offset values**. The exploration was done in two steps: on the coarse grid of foot parameters to get a region of the optimum (top) and on the dense grid to refine the optimum (down). The process was repeated for two frequencies: 0.5Hz (left) and 0.75Hz (right).

Extended Data 10: **Computation of the precision metric** (Supplementary Information 1). (Top) The idealized trackways (Extended Data 1k) and the robot footsteps extracted from Webots simulation were not necessarily aligned in the world reference frame, since the robot did not use path-following strategies. (Middle) The trackways and the footsteps were approximately aligned by matching their centrelines via translation and rotation. (Bottom) A precise alignment was done by translation, whose amount was determined through an optimization that minimized distances between the corresponding footsteps. The remaining distances were summed and used as a measure of precision.

## METHODS

**Comparative motion analysis of extant species.** All procedures involving live animals adhered to animal welfare regulations and were authorized by the responsible authorities in Thuringia (Thüringer Landesamt für Verbraucher- und Umweltschutz), Germany (registration number: 02-008/11). All specimens were adult and did not show any abnormalities. The experimental design combined biplanar, high-speed x-ray videography with the simultaneous measurement of single limb ground reaction forces (GRFs) to investigate locomotor mechanics. Additionally, trackway production was quantified during locomotion on soft clay (i.e., in a similar situation as preserved fossil trackways assigned to *Orobates*<sup>8</sup>). Kinematic analysis was conducted using the x-ray facility of the Institut für Zoologie und Evolutionsforschung at the Friedrich-Schiller-Universität in Jena, Germany. The specifics of the facility have been described in previous publications<sup>28,29,30</sup>. Synchronized x-ray recordings from ventral and lateral projections of locomotor trials in which the animals could choose the speed of progression were captured using 38 cm diameter image intensifiers at a resolution of 1536 x 1024 pixels. Locomotion, if not exhibited spontaneously, was motivated by gentle touches with a stick on the tail resulting in a series of several consecutive strides. For the salamanders and skinks we used an instrumented trackway (1.0 x 0.3 m) and for the iguanas and caimans a larger trackway was built (3.0 x 0.75 m). Both instrumented trackways were built with the force plates integrated flush with the trackway. Both the small and the large trackway had an acrylic glass enclosure. Recording frame rate varied from 300 frames per second (fps) for salamanders to 500 fps (other species).

For x-ray motion analysis, we used the non-invasive variant of x-ray reconstruction of moving morphology (XROMM; no need to implant metal markers into bones of interest) termed “scientific rotoscoping” (SR<sup>31,32</sup>). The general procedure for SR was identical for the analysis of all sampled subjects and was described in detail in a previous publication<sup>33</sup>. In SR a digital 3D model of the subject’s skeletal elements of interest is manually positioned to match (i.e., overlay) these elements’ x-ray shadows in both x-ray projections. For this, the 3D animation software Autodesk Maya® 2015 (Autodesk, San Rafael, CA, USA) was used. The manual matching of 3D bone models with x-ray shadows was repeated for key frames (usually 15-20 keyframes each for the stance and swing phase) of the x-ray video and was then cubic-spline interpolated between keyframes to produce smooth movements that closely approximate the recorded skeletal kinematics. Raw x-ray videos were corrected for distortion prior to SR<sup>32</sup> and the distance/orientation of the x-ray image intensifiers in relation to the subject was determined by using a calibration object (0.2x0.12x0.12 m) placed within the biplane field of view. We used the Matlab® (The MathWorks, Inc. Natick, MA, USA)

calibration routine developed at Brown University, Providence, USA ([www.xromm.org](http://www.xromm.org)). To obtain bone models, CT scans were done either on a CT scanner belonging to the Friedrich-Schiller-University Hospital, Jena, Germany (skinks, iguanas, and caimans), or on a microCT scanner at the Fritz Lipmann Institute, Jena, Germany (salamander cadavers). Living skinks and iguanas were cooled to ca. 15°C to reduce movement and caimans were scanned inside a dark transport box. Sedation was not necessary. Bone surface models were obtained using the segmentation editor in the Amira® software package (VSG, Burlington, MA, USA).

In SR, bone models are linked to form a hierarchical marionette in Maya® (Maya® tools available at [www.xromm.org](http://www.xromm.org))<sup>32</sup>. Anatomical coordinate systems were implemented into the shoulder and pelvic girdle models of all species to measure the rotation of each girdle about a dorso-ventral axis as well as into the shoulder and hip to measure LAR, retraction, and abduction/adduction as described previously<sup>33</sup>. Movements in the shoulder and hip were measured relative to the respective girdles using anatomically defined joint coordinate systems (JCS)<sup>32</sup>. We quantified the rotations (3 degrees of freedom, DOF; equivalent of a ball and socket joint) in the shoulder and hip joints relative to a reference pose. This pose was aligned to a right-handed global coordinate system placed in the trackway with positive x axis pointing in the direction of movement, positive y axis pointing to the animals' left, and positive z axis pointing upwards. All bone model JCS were aligned to the axes of the global coordinate system<sup>30,33</sup>. To obtain anatomically meaningful data we used non-physiological fully extended reference poses (for both the fore and the hindlimbs; with the humerus and femur pointing laterally<sup>29,37,34,35</sup>. To avoid the singularity problem, the rotation order in each JCS was set to have the largest expected movement as the dominant axis (cf.<sup>34</sup>, rotation order: z, y, x). All data were exported into Microsoft Excel® (v. 2014, Microsoft, Redmond, WA, USA) and each trial was normalized to the same duration (101 points). LAR/retraction of the shoulder and hip joints and spine bending was quantified as the range (from min to max) occurring during a limb's ground contact. Body height (at midstance measured as distance from the spine at the shoulder or hip to the ground) and track parameters (stride length and width) were normalized to inter-girdle distance (IGD) to allow comparison across all specimens (also including the kinematic and dynamic simulations).

We ran multiple linear regression (MLR) with LAR (in shoulder and hip), body height, retraction and spine bending as either dependent or independent variables (i.e., 3 degrees of freedom) in Microsoft Excel® using the "data analysis" add-in to statistically assess our qualitative observations. *P* values were considered significant if below 0.05.

Custom-built force plates made from carbon fibre with 6 DOF force-torque transducers (ATI®, Industrial Automatization, Apex, NC, USA) were used to measure vertical GRFs in

skinks and salamanders. For the caimans and iguanas, vertical GRFs were collected using a radiotranslucent board mounted on two Kistler® (Kistler Group, Winterthur, Switzerland) force plates which were placed at both sides of the trackway to allow ventro-dorsal x-ray projection. Details of the design of the force plates used and GRF data analysis are documented in<sup>30,33,36</sup>. Vertical GRFs were collected at 500 Hz using customized software for LabView® 2009 (NI USB-6229, National Instruments Corp., Austin, TX, USA). GRFs were normalized to body weight units (BWUs). GRFs were also used to estimate the external moment acting on the shoulder joint at the instant of peak vertical force (see<sup>33</sup> for detailed explanation). Assuming a quasi-static situation, the external moment needs to be counteracted by an equal and opposite joint torque. We compared dimensionless joint torques across species (and the robot) by dividing absolute joint torques by the product of body mass, gravitational acceleration and humeral length (Supplementary Data 12).

To document track production during walking while being recorded by a high-speed camera, trackways were custom built for each species (see previous publication<sup>37</sup>). In the centre of each trackway a bed of fine pottery clay (100x30x2 cm) and a measuring tape were placed within the field of view of the camera. The camera (Photron® FASTCAM-X 1024PCI, Photron USA, Inc., San Diego, CA, USA) was positioned to capture a dorsal view. After each trial the imprints were photographed with a resolution of 4000 x 3000 pixels (Canon® Powershot G9, Canon Inc., Tokyo, Japan). Stride length, stride width, and pace angulation were determined from photographs using ImageJ software (<http://rsbweb.nih.gov/ij/>). Only trials on clay with relatively equal moisture contents (using qualitative categories see<sup>37</sup>) were used for data analysis. Video data were used to determine locomotor speed (determined by measuring the displacement of the snout in direction of travel over a stride cycle).

**Digital marionette design and kinematic simulation of *Orobates*.** Fossil trackways were digitized, imported into Maya® and idealized so that two subsequent stride cycles were repeated infinitely (using an animated loop) and animated as if on a treadmill (Extended Data 2). The digital holotype specimen of *Orobates*<sup>17</sup> was also imported into the scene. The digital marionette was scaled using the 'scale' tool so that the hands and feet of the fossil visually matched the size of the imprints. To allow simulated movement of the digital skeleton, it was rigged using Maya's 'joints' and 'bones' tools to form a digital marionette in which in principle all anatomical joints can be controlled by the user via the underlying Maya 'joints'. A generic (default) locomotor sequence was achieved by using kinematics observed in the extant species and accounting for measurements taken in the motion analysis of extant species for spine bending, LAR and retraction at the shoulder and hip joints. Previously estimated joint ranges of motion in the shoulder and hip<sup>17</sup> were not violated by the

default sequence. We simplified animation of most joint movements using Maya's inverse kinematics solvers (see<sup>10,38</sup> for general introduction into inverse kinematics in 3D animation) for the spine, each limb, and roll-off motion of the hands and feet qualitatively approximating movements observed in extant species. Hands and feet were forced to contact the ground with limb phase of 0.5, D of 0.75, and a stride frequency of 0.75 (i.e. an idealized walking trot as was occasionally exhibited by all extant species studied). Critically, the simulation allowed user-specified systematic variation of the kinematic parameters within the sprawling gait space (SGS), namely body height (from belly-dragging to more erect postures via abduction/adduction in the shoulder and hip), spine bending (from none to exaggerated via rotation about a dorsal ventral axis in the girdles), and LAR and retraction in the shoulder and hip joints (Extended Data 2). For each resulting parameter combination, anatomical plausibility was evaluated by a kinematic metric checking for bone collisions in the shoulder and hip joints and the spine, as well as for disarticulation of wrist and ankle joints during the stride cycle (if at all, then usually occurring at the beginning or end of a limb's ground contact). We used a graded score ranging from 1 (disarticulation of joints and/or definite bone collisions) to 4 (no disarticulations and bone collisions) with 2 and 3 scored for minimal and moderate bone collisions, respectively, evaluated by one of the investigators (JAN). Soft tissues were not modelled. Since collisions in joints not controlled by user specification may occur due to unspecified joint kinematics found by the inverse kinematics solver, all other bone collisions were not taken into account. Similarly, swing phases were animated, but not taken into consideration.

**Robot design:** We followed the robot design methodology of Pleurobot in our previous work<sup>23</sup>, but designed OroBOT to account for the anatomy of *Orobates* (Extended Data 1a-c). To recreate the spine, we segmented it in 8 actuated joints: 2 for the neck, 4 for the trunk, and 2 for the tail. All joints were coplanar and rotated in the coronal plane (parallel to the ground). The tail was connected through a passive joint in the sagittal plane and cantilevered so it did not touch the ground, because no evidence of tail dragging is apparent in the fossil trackways<sup>8</sup>. Each limb contained 5 actuated joints: 3 shoulder/hip joints in a spherical configuration (protraction-retraction, abduction-adduction, LAR), an elbow/knee joint (extension-flexion), and a wrist/ankle joint for foot rotation (Extended Data 1d). OroBOT's 3D printed parts were fabricated using selective laser sintering (SLS) with polyamide plastic as material. The parts were designed in Inventor® 2017 (Autodesk, San Rafael, Ca, USA) and provided the structural attachments for the servo motors. We used 24 Dynamixel (Robotis Inc., Seoul, Korea) MX-64R servomotors (8 in spine and 4 for each limb) and four Dynamixel MX-28R servomotors for the wrist and ankle rotation. All motors were connected using the standard Dynamixel cables and communication protocol, except for distributed power loops

to prevent voltage drops from a 14.8V power supply. To control the robot, we used a Odroid XU4 Linux Computer (Hardkernel co. Ltd. GyeongGi, Korea). Each OroBOT foot consisted of three passive compliant joints. The palm and fingers were approximated by a rectangular shape. The size was chosen so the rectangle lies within the footprint area. Width, palm and finger lengths were 8.7x5.7x4.5 cm for the front foot (manus), and 9.1x6.1x5.1 cm for the hind foot (pes) (Extended Data 1e). The passive joints corresponded to the wrist and ankle joints (foot dorsiflexion-plantar flexion and eversion/inversion) and the metacarpal-phalangeal and metatarsal-phalangeal joints, respectively (Extended Data 1f). These joints were elastic to make the foot comply with the ground, guaranteeing a full foot contact, and also to be able to reset its original state between the steps (Supplementary Information 11, Extended Data 9). The foot, including the three passively compliant joints, was designed in Inventor® and fabricated using four layers of 1mm Polyethylene terephthalate (PET), cut with a Speedy400 Flexx™ laser cutter (Trotec Laser GmbH, Marchtrenk, Austria). The four layers were bonded together with a stretched rubber layer and fixed to the robotic limb with screws. The cutout profile on each foot layer was designed to allow bending in the required rotation axes (Extended Data 1e). Coefficients of elasticity were primarily approximated with finite element analysis in Inventor®, and then iterated to find a good trade-off between matching the expected stiffness value and the admissible bending without breaking or plastic deformation failure of the PET material. Because of actuator constraints, the robot was scaled to 1.6 times the size of the fossil (85.14 cm), for a length of 136.22 cm. An additional scaling of 1.4 was applied to the fossil head (11.14 cm) to provide space for the computer and peripherals, increasing the total length to 143.35 cm. Except for the head, all the lengths were geometrically scaled, respecting the same aspect ratios of the fossil reconstruction (Extended Data 1a,b). Correct geometrical scaling was validated by comparing relative ratios of OroBOT segment lengths with respect to body length, to those of *Orobates* (Extended Data 1c). Discrepancies remained less than 2.05% (Extended Data 4c).

**Mass distribution:** Mass should scale with the power of three of the length scale to achieve a correct dynamic scaling<sup>39</sup>. In OroBOT, this results in a four-fold mass increment. As the servo motors' maximal torque was not enough to smoothly execute gaits with such a weight, we decreased OroBOT's mass (M=6.189 kg) to be only 1.5 times *Orobates*'s mass (M=3.981 kg), yet maintaining the same mass distribution. We averaged maximum and minimum reported plausible masses<sup>17</sup> of *Orobates*'s head, neck, front limbs, trunk (comprised by pectoral girdle, spine segments and pelvic girdle), hind limbs and tail. We computed relative mass of each segment against the total mass (Extended Data 1c). The 3D printed parts of OroBOT were designed, and its servomotors located, in order to comply with

the same mass distribution ratios. Discrepancies were found to be less than 1% (Extended Data 4a).

**Dynamic robot simulation.** The simulated OroBOT was created in Webots™ V8.5.4. (Cyberbotics Ltd, Lausanne, Switzerland) The simulation was tuned to represent real physical quantities of the robot-like size and mass distribution. The ground was represented as a horizontal plane. The coulomb friction coefficient between robot's feet and the ground was set to 0.4, which resulted in a reasonable amount of slipping across multiple gaits. The integration time step of the built-in physics engine was 2 ms. The controller loop ran at a frequency of 100 Hz which corresponded to the control setup on the real robot. The simulated robot was equipped with the following sensors: inertial measurement unit (IMU), joint encoders, joint torque sensors and position trackers (simulated GPS). The IMU was placed in the front (pelvic) girdle and it provides body roll and pitch angles. The position trackers were placed on each foot, providing their position in the world frame. The sensor readings were logged to a text file at the rate of the controller loop execution. Due to the complexity of simulating an elastic material, the manus and pes were approximated with two rigid bodies, representing the proximal elements (carpus/tarsus) and digits, connected by a passive joint. It was attached to the leg via two passive joints with axes of rotation (Extended Data 1d). The passive joints were modelled as spring-damper systems with tunable parameters (Supplementary Information 11).

**Walking frequency:** As it is impossible to measure the speed or stride frequency in *Orobates*, we used the dynamic similarity hypothesis<sup>40</sup> to define a walking speed for OroBOT. Data from diverse animals with a sprawling posture (Extended Data 3b) were used to compute the Froude number ( $Fr=h(f)^2g^{-1}$ ). We used the stride length as characteristic length  $h$ , the gait frequency  $f$  and gravity  $g$ . Unlike other approaches, we did not use the hip height as characteristic length [<sup>40</sup>], due to the sprawling posture nature of the gaits. Froude numbers from the  $n=19$  specimens (8 species) analyzed ranged from 0.4 to 3.92 with a mean of 1.42. Similarly, we calculated the Froude number for OroBOT at admissible frequencies within the speed range of the servomotors  $f=[0.25, 0.5, 0.75, 1]$  Hz. The respective Froude numbers  $Fr=[0.31, 1.22, 2.75, 4.88]$  were found. We chose to use 0.5 Hz and 0.75 Hz to be walking frequencies for our gait reconstruction because they were within the Froude number range of the analyzed extant species. In order to test whether the stride frequencies used for OroBOT resulted in realistic frequencies in *Orobates*, based on the Froude numbers used in OroBOT we calculated the corresponding frequencies for *Orobates*. We found  $f=[0.3, 0.6, 0.9, 1.3]$  Hz, which are within the range of the data observed in extant sprawling species. As a final verification, we also analyzed the relationships between the

Froude number and both the duty factor and limb phase differences as suggested by the dynamic similarity hypothesis<sup>40</sup>. The data obtained when these relationships were calculated for the n=19 specimens fall consistently into a similar range of values to those of the robot.

**Locomotion control of OroBOT.** OroBOT was controlled by providing position reference signals to its 28 servo motors. The control was based on solving the inverse kinematics of the legs and the spine in order to produce a desired gait. Each leg formed a kinematic chain that started at the girdle and ended at the foot. The trunk was a planar kinematic chain that connected the front and hind girdles. Synchronization between legs and spine was provided by an upper layer of the controller, which was a trajectory generator; thus the inverse kinematics of each kinematic chain could be solved separately. To solve the leg inverse kinematics, we used an iterative Jacobian pseudoinverse method<sup>41</sup> and formulated the problem as a quadratic program allowing us to include joint limits as constraints. Since the number of leg (excluding the wrist/ankle) degrees of freedom (four) was higher than the number of coordinates defining the foot position (three), the solution of inverse kinematics was not unique. The extra degree of freedom was used to adjust the leg posture, which indirectly affected the amount of LAR during walking. The problem was solved numerically using qpOASES solver<sup>42</sup> (Supplementary Information 3). The method was not suitable to solve the inverse kinematics of the spine due to a presence of kinematic singularities (straight spine). Thus we used the same method as in<sup>43</sup> that relied on spline approximation and fine adjustments through optimization by using a nonlinear solver from the Dlib library<sup>44</sup> (Supplementary Information 4). A foot trajectory was described as a parametrized closed curve in the robot's frame of reference. As the feet were complex, with multiple points touching the ground simultaneously, the trajectory referred to the proximal attachment point of a foot (i.e. wrist/ankle). The overall robot motion was the consequence of all feet executing such trajectories at their respective timings. The spine trajectory described the orientation of the girdles in time, which resulted in spine bending (Supplementary Information 4-8 and Extended Data 8). Measurements acquired from the trackways were used to determine values of the parameters linked with gait kinematics like stride width, length and distance between ipsilateral footprints (Supplementary Information 9). Values of the remaining gait parameters (e.g. limb phase offset or duty factor D), that could not be inferred from the trackways, were chosen to be biologically reasonable taking into account quantities present in extant animals (Supplementary Information 10).

**Gait exploration and evaluation.** Each of the three main gait parameters of the SGS (Supplementary Information 8) was assigned eight different values, resulting in n=512 evaluated gaits. The evaluation consisted of (i) simulating the robot for a specific parameter

combination, (ii) logging the data relevant for the metrics, (iii) processing the data to evaluate the individual metrics power expenditure, balance, precision and GRF for each gait (see Supplementary Information 1,2, Extended data 10). All data processing was done in Matlab® R2016b. To evaluate each gait, the individual metrics had to be combined. The easiest way would be to use an average score of each gait across the four (normalized) metrics. Such an approach could skew the results towards gaits with a disproportionately high score (an outlier) compared to others in a single metric. To avoid giving too much relevance to a single metric or small variations within it, we adopted and modified the constraint-based exclusion approach<sup>11</sup>. To achieve this, each metric was also assigned an exclusion score. The exclusion score was formed by giving a score of 1 to the gaits that performed better than a user-defined threshold in a respective metric. The remaining gaits were “excluded” by giving them a score of 0. The threshold for each metric was calculated as a K-th percentile to assure each metric had the same score distribution. In Fig. 3, we used K=50, which corresponds to the median value. To combine the metrics, the exclusion scores were summed. The gaits which passed thresholds in all the four metrics had the maximum score of 4. Such approach favoured gaits that scored “well enough” across all the metrics (as opposed to gaits that score highly in one metric but not in others). In the final step, the identified anatomically plausible gaits (kinematic simulation) and the dynamically plausible gaits (OroBOT simulation) were combined to find gait solutions for *Orobates* in the SGS.

**Validation of kinematic and dynamic simulation workflows.** To validate the inference of anatomical plausible gaits for *Orobates* and the kinematic metric, we followed the same workflow, namely predicting the plausible gaits of the spectacled caiman in SGS using only its morphology and trackway data for a disarticulated *Caiman crocodilus* specimen (inventory no.: PMJ Rept 665) housed at the Phyletisches Museum Jena, Germany, and compared the results to the actual kinematics measured during our caiman x-ray motion analysis (Supplementary Data 12). First, CT-scans of the specimen were obtained. Bone surface models were generated using Amira® software and the high-detail meshes were reduced using the ‘remesh’ tool in ZBrush® (Pixologic, Los Angeles, CA, USA). Trackway information (from a photograph) of a representative trial of the female caiman specimen was imported from the trackway analysis of the extant species into Maya® and digitized as described above for trackways assigned to *Orobates*. After import of both models (i.e. digital skeleton and digitized trackways) into Maya®, the caiman skeleton was ‘rigged’ and animated in the same way as *Orobates*. Note that for the default stride cycle the available x-ray videos of the caiman were not used. In analogy to the *Orobates* workflow, n=100 parameter combinations of body height, spine bending, and LAR/retraction were tested for anatomical plausibility in the hind limbs (identical scoring as used during the *Orobates*

kinematic simulation). Comparison to the actual kinematics during slow high walks of caimans during the x-ray motion analysis (the caimans did not exhibit any low walks) demonstrated that the anatomically plausible gait parameter combinations identified in the SGS by our workflow encompassed the actual quantified motion data of living caimans, thus validating the kinematic simulation workflow (Extended Data 5). We further validated our dynamic simulation approach and tested its predictive power of finding a “plausible gait region” within the SGS for an extant animal using only its morphology and its trackway parameters. Using an extant sprawling animal was crucial in this validation, because it provided us with both inputs needed for our approach (animal kinematics, trackways) and the output (gait location within its own SGS). The chosen animal was the Spanish ribbed newt *Pleurodeles waltl* because we already had its robotic representation in the form of Pleurobot<sup>23</sup> and data needed for the workflow (Supplementary Data 13). *Pleurodeles* trackways were extracted from a top-view x-ray video of the animal walking. The trackways were used to constrain the gait parameters of Pleurobot in the same way it was done with OroBOT. The walking frequency of Pleurobot was set to 0.25 Hz to achieve a dynamic similarity between the animal and the robot<sup>23</sup>. The trajectory shift and parameters of the feet were found following the same procedure as with OroBOT. Examination of the resulting metrics for n=512 gaits revealed that all four metrics, after excluding all gaits with low scores (threshold set to 50th percentile), were successful in predicting the region containing the *Pleurodeles* gait (Extended Data 6).

**Code availability.** Webots and Matlab code can be found in the GIT repository ([https://gitlab.com/thorvat27/orobot\\_dynamic\\_simulation](https://gitlab.com/thorvat27/orobot_dynamic_simulation)).

28: Fischer, M. S., Krause, C., & Lilje, K. E. (2010). Evolution of chameleon locomotion, or how to become arboreal as a reptile. *Zoology*, 113(2), 67-74.

29: Nyakatura, J. A., & Fischer, M. S. (2010). Functional morphology and three-dimensional kinematics of the thoraco-lumbar region of the spine of the two-toed sloth. *Journal of Experimental Biology*, 213(24), 4278-4290.

30: Andrada, E., Nyakatura, J. A., Bergmann, F., & Blickhan, R. (2013). Adjustments of global and local hindlimb properties during terrestrial locomotion of the common quail (*Coturnix coturnix*). *Journal of Experimental Biology*, 216(20), 3906-3916.

31: Brainerd, E. L., Baier, D. B., Gatesy, S. M., Hedrick, T. L., Metzger, K. A., Gilbert, S. L., & Crisco, J. J. (2010). X-ray reconstruction of moving morphology (XROMM): precision, accuracy and applications in comparative biomechanics research. *Journal of Experimental Zoology Part A: Ecological and Integrative Physiology*, 313(5), 262-279.

32: Gatesy, S. M., Baier, D. B., Jenkins, F. A., & Dial, K. P. (2010). Scientific rotoscoping: a morphology-based method of 3-D motion analysis and visualization. *Journal of Experimental Zoology Part A: Ecological and Integrative Physiology*, 313(5), 244-261.

- 33: Nyakatura, J. A., Andrada, E., Curth, S., & Fischer, M. S. (2014). Bridging “Romer’s Gap”: limb mechanics of an extant belly-dragging lizard inform debate on tetrapod locomotion during the early carboniferous. *Evolutionary Biology*, 41(2), 175-190.
- 34: Sullivan, C. S. (2007). *Function and evolution of the hind limb in Triassic archosaurian reptiles*. Harvard University.
- 35: Nyakatura, J. A., & Fischer, M. S. (2010). Three-dimensional kinematic analysis of the pectoral girdle during upside-down locomotion of two-toed sloths (*Choloepus didactylus*, Linné 1758). *Frontiers in Zoology*, 7(1), 21.
- 36: Witte, H., Biltzinger, J., Hackert, R., Schilling, N., Schmidt, M., Reich, C., & Fischer, M. S. (2002). Torque patterns of the limbs of small therian mammals during locomotion on flat ground. *Journal of Experimental Biology*, 205(9), 1339-1353.
- 37: Curth, S., Fischer, M. S., & Nyakatura, J. A. (2014). Ichnology of an extant belly-dragging lizard— analogies to early reptile locomotion?. *Ichnos*, 21(1), 32-43.
- 38: Watt, A., & Watt, M. (1992). Forward vs inverse kinematics in computer animation. *Advanced animation and rendering techniques*, 371-384.
- 39: Alexander, R. McN. *Principles of Animal Locomotion*. (Princeton University Press, 2013).
- 40: Alexander, R. M., McN. Alexander, R. & Jayes, A. S. A dynamic similarity hypothesis for the gaits of quadrupedal mammals. *J. Zool.* 201, 135–152 (1983).
- 41: Buss, S. R. (2004). Introduction to inverse kinematics with jacobian transpose, pseudoinverse and damped least squares methods. *IEEE Journal of Robotics and Automation*, 17(1-19), 16.
- 42: Ferreau, H. J., Kirches, C., Potschka, A., Bock, H. G. & Diehl, M. qpOASES: a parametric active-set algorithm for quadratic programming. *Math. Program. Comput.* 6, 327–363 (2014).
- 43: Horvat, T., Melo, K. & Ijspeert, A. J. Spine Controller for a Sprawling Posture Robot. *IEEE Robotics and Automation Letters* 2, 1195–1202 (2017).
- 44: King, D. Dlib C++ library. Available at: [dlib.net/](http://dlib.net/). (Accessed: 5th February 2018)
- 45: Jagnandan, K., Russell, A. P. & Higham, T. E. Tail autotomy and subsequent regeneration alter the mechanics of locomotion in lizards. *J. Exp. Biol.* 217, 3891–3897 (2014).
- 46: Reilly, S. M. & Elias, J. A. Locomotion in alligator mississippiensis: kinematic effects of speed and posture and their relevance to the sprawling-to-erect paradigm. *J. Exp. Biol.* 201, 2559–2574 (1998).
- 47: Rome, L. C. Energetic Cost of Running with different Muscle Temperatures in Savannah Monitor Lizards. *J. Exp. Biol.* 99, 269–277 (1982).
- 48: Jagnandan, K. & Higham, T. E. Lateral movements of a massive tail influence gecko locomotion: an integrative study comparing tail restriction and autotomy. *Sci. Rep.* 7, 10865 (2017).
- 49: Reilly, S. M., McElroy, E. J., Odum, R. A., & Hornyak, V. A. (2006). Tuataras and salamanders show that walking and running mechanics are ancient features of tetrapod locomotion. *Proceedings of the Royal Society of London B: Biological Sciences*, 273(1593), 1563-1568.
- 50: Horvat, T., Karakasiliotis K., Melo K., Fleury L., Thandiackal R. & Ijspeert A. J. Inverse kinematics and reflex based controller for body-limb coordination of a salamander-like robot walking on uneven terrain. *IEEE/RSJ International Conference on Intelligent Robots and Systems (IROS)*, 195-201 (2015).

# Data acquisition



body fossil of *Orobates*

CT-based  
3D reconstruction  
of bones

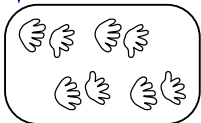


digital model of  
*Orobates*



fossil trackways  
assigned to  
*Orobates*

digitalization



digital model of  
*Orobates* trackways



extant sprawling  
tetrapod  
species

x-ray motion  
analysis and GRF



animal data

anatomical and gait  
constraints for simulation

OroBOT robot  
design

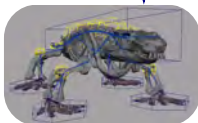
digital marionette  
design

# Simulation

validation



dynamic OroBOT  
simulation



kinematic *Orobates*  
simulation

mechanical  
principles of  
sprawling  
locomotion

dynamic  
filters

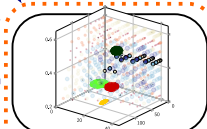
kinematic  
filter

animal  
data



OroBOT walking matching  
*Orobates* trackways

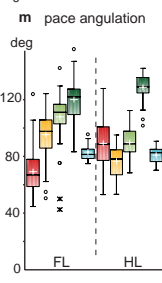
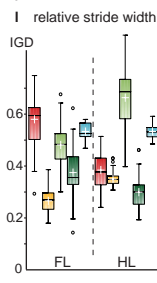
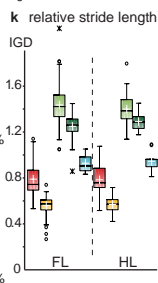
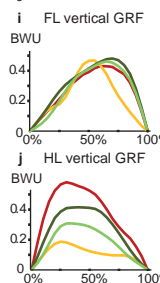
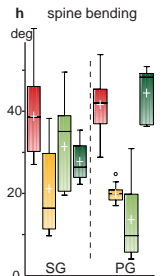
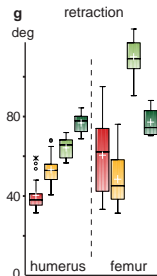
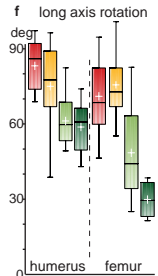
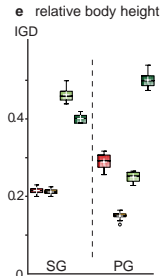
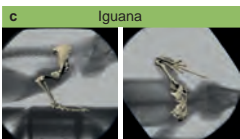
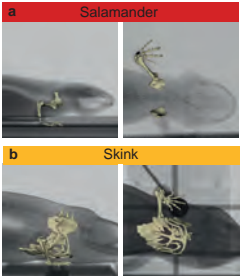
proof of  
concept

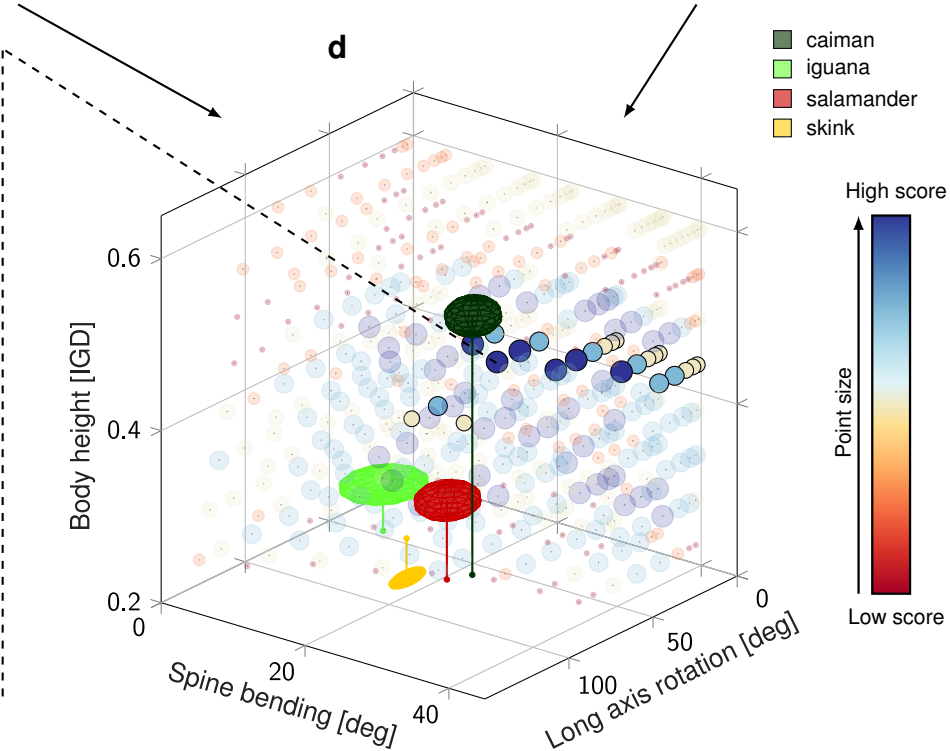
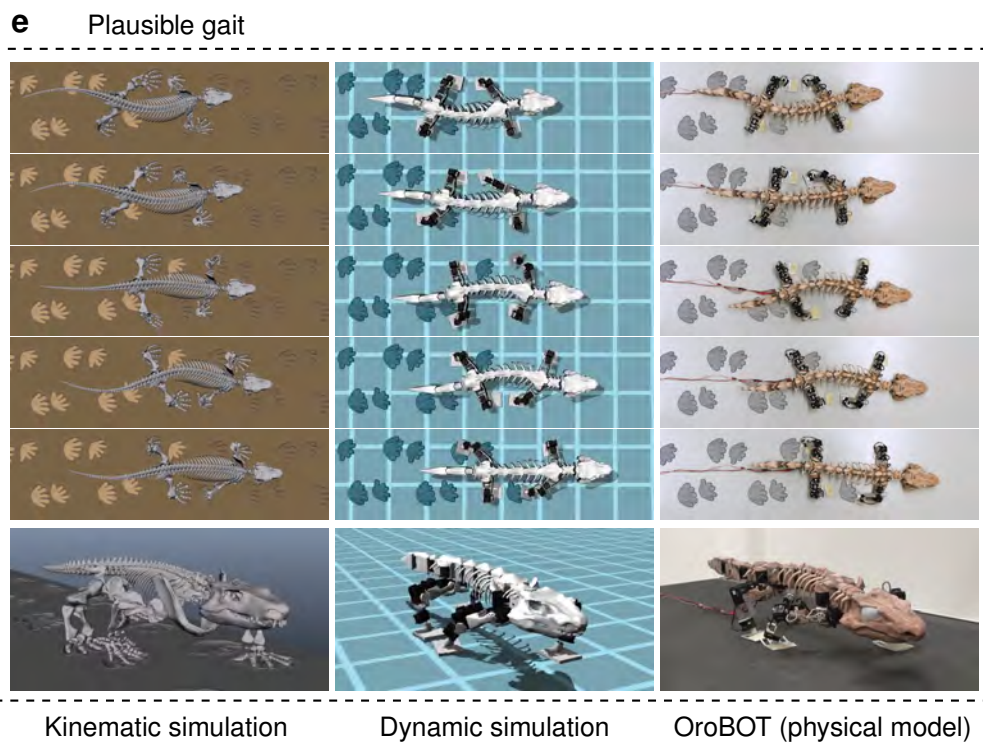
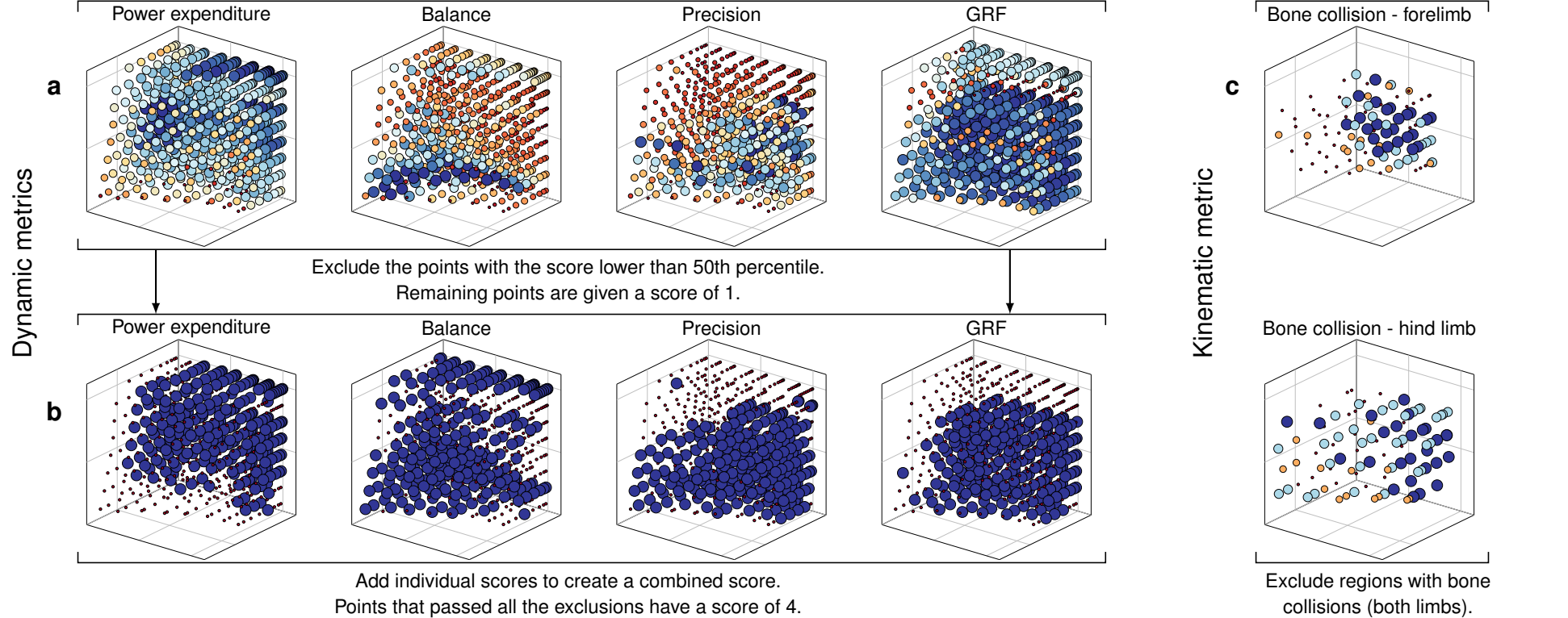


*Orobates* gait solutions in  
sprawling gait space (SGS)

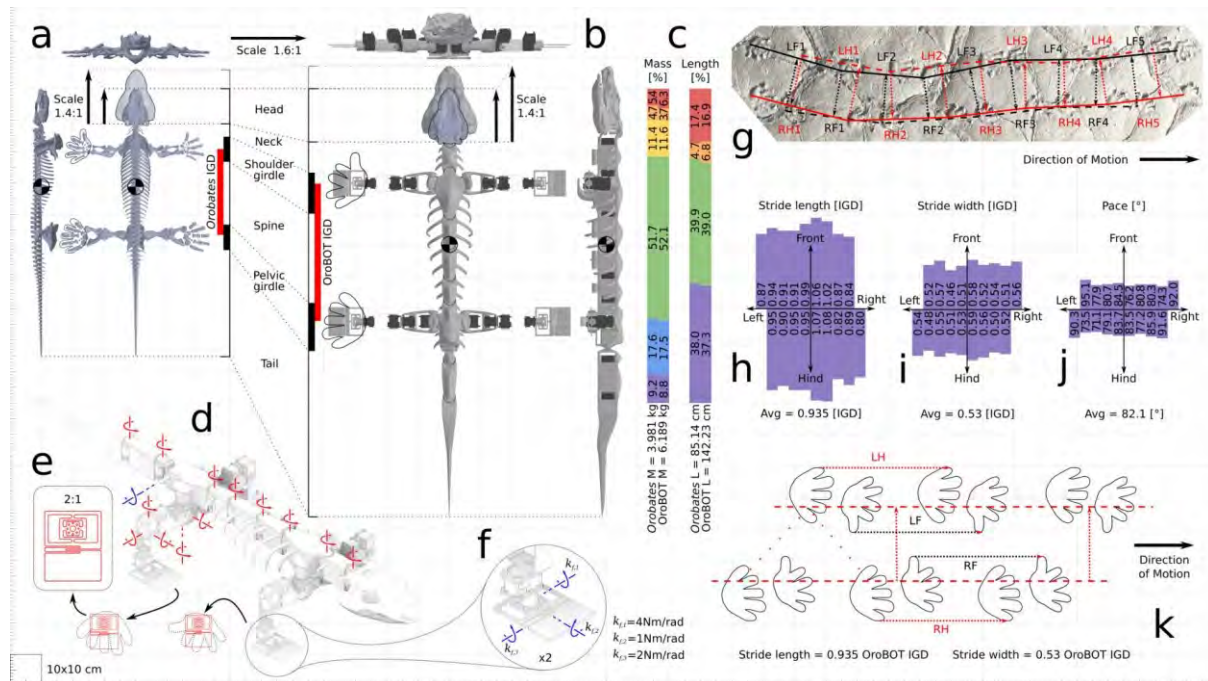
## Robotics

## Gait solutions

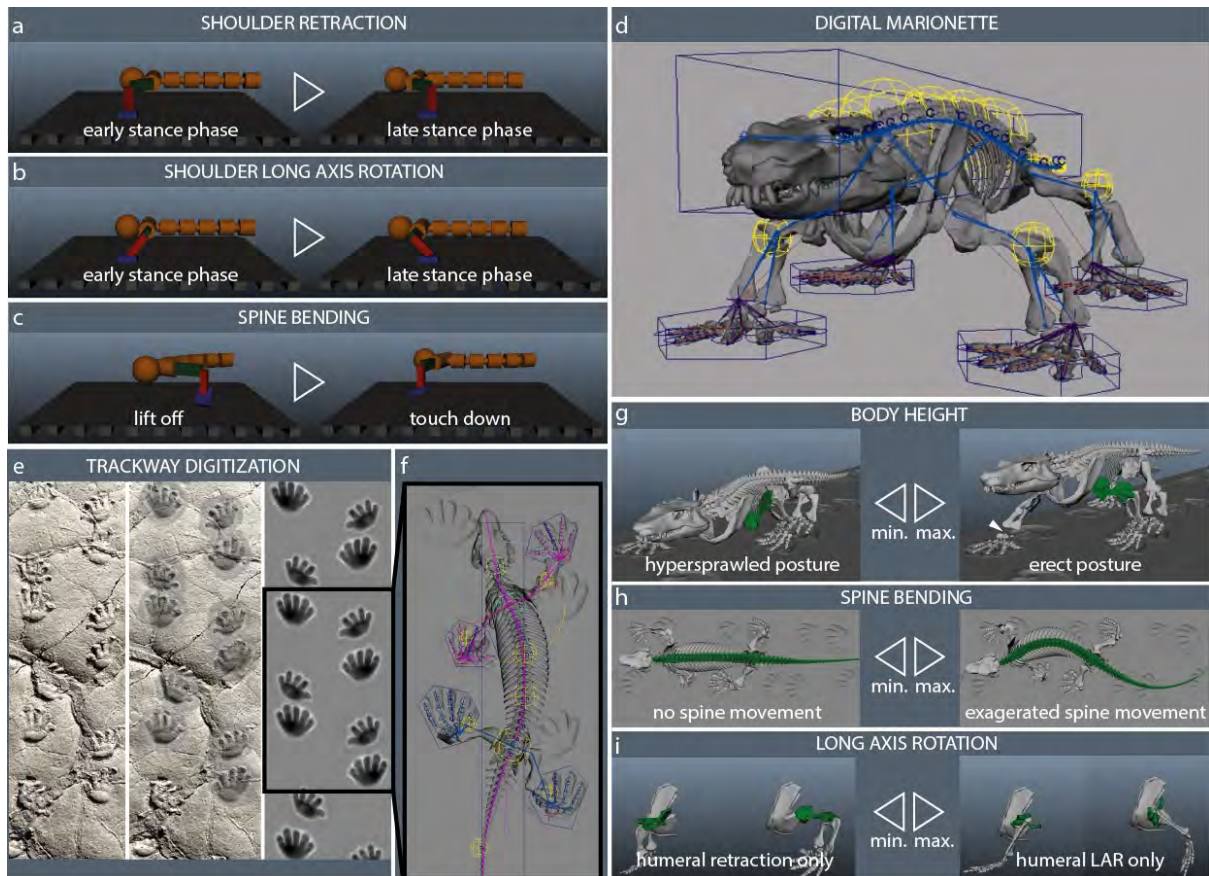




## EXTENDED DATA



Extended Data 1: **Fossil, robot, and trackway detailed description (10x10 cm grid).** (a) *Orobates* fossil 3D views. Position of centre of mass<sup>17</sup> and lengths of different segments including inter-girdle distance (IGD) in red bar. (b) Scaled (1.6:1) robotic reconstruction of *Orobates* fossil called OroBOT. 3D views, position of centre of mass, segment lengths and scaled IGD in red bar. Details of head secondary scale for housing the processing unit volume. (c) Mass and length distributions and comparison between different segments of fossil used for the robot design. Fossil masses and lengths percentages matching in the robotic replica (Extended Data 4a-c). (d) Isometric view of OroBOT robot specifying the joints location. Active joints (28 in total) in red and passive joints in blue. (e) Passive compliant hind foot pattern (scaled 2:1), comparison with footprints from fossil tracks, and physical implementation in the robot. (f) Detail of the passive compliant foot with stiffness values for each of the bending axes. (g) Original *Orobates* - associated trackway (MNG 1840), not showing any signs of slipping or tail use during locomotion. (h) Detail of stride lengths, (i) stride widths, and (j) pace measurements for front, hind, left and right feet in (g). (k) Idealized trackway for OroBOT (Extended Data 2f). Stride length, stride width and pace (i.e., the angle between three consecutive imprints of alternate feet) correspond to averaged values of the data in (h), (i), and (j)  $n=18$  in each case.



Extended Data 2: **Kinematic simulation of *Orobates***. **(a-c)** The generation of body propulsion during sprawling tetrapod locomotion (exemplified for a forelimb). **(a)** The humerus (dark green) is retracted in the shoulder joint. **(b)** The humerus is rotated about its long-axis in the shoulder joint. Both mechanisms also apply to the hind limb (femoral movement relative to the hip). **(c)** Spine bending during the swing phase contributes to step length. **(d)** Fully “rigged” version of the digital *Orobates* reconstruction allowing for systematic variation of body height, LAR and retraction in the shoulders and hips, and spine bending. **(e)** Digitization and idealization of trackways (MNG 1840) for kinematic simulation. Manus (hand) and pes (foot) imprints were idealized and superimposed to fossil trackways to retain stride length, stride width, pace angulation, and manus and pes rotation. **(f)** Enlarged portion of the idealized trackway with digital reconstruction of the *Orobates pabsti* holotype specimen placed into the trackway. **(g-i)** Systematic exploration of the kinematic parameter space. Plausibility of a parameter combination was ruled out if it resulted in bone collision within the spine or within the shoulder and hip joints as well as when disarticulation of limb joints occurred (see white arrowhead in **(g)**). **(g)** Body height. **(h)** Spine bending. **(i)** Long axis rotation (LAR).

**a**

Species	Sex	Mass [g]	TL [mm]	IGD [mm]
<b>Mexican salamander (<i>Ambystoma mexicanum</i>)</b> hindlimb to snout vent length ratio: approx. 0.3 forelimb to hindlimb length ratio: approx. 0.85	Female	58.9	194	82
	Female	72.6	194	81
	Male	66.5	205	88
	Male	67.6	239	92
<b>Blue tongued skink (<i>Tiliqua scincoides</i>)</b> hindlimb to snout vent length ratio: approx. 0.17 forelimb to hindlimb length ratio: approx. 1.0	Female	1,150	560	240
	Male	965	540	210
<b>Green iguana (<i>Iguana iguana</i>)</b> hindlimb to snout vent length ratio: approx. 0.75 forelimb to hindlimb length ratio: approx. 0.67	Female	1,450	1160	190
	Male	2,010	1250	210
<b>Spectacled caiman (<i>Caiman crocodilus</i>)</b> hindlimb to snout vent length ratio: approx. 0.39 forelimb to hindlimb length ratio: approx. 0.75	Female	10,010	1260	360
	Male	9,700	1370	380
<b><i>Orobates pabsti</i> (MNG 10181)*</b> hindlimb to snout vent length ratio: approx. 0.4 forelimb to hindlimb length ratio: approx. 0.9	Unknown	3,981	851	273

**b**

	a	b	c	d	e	f	g	h	i	j	k	l	m	n	o	p	q	r	s
Limb phase	0.44	0.42	0.44	0.36	0.70	-	-	0.53	0.37	0.48	0.57	-	-	-	-	-	-	-	-
Duty factor	0.61	0.63	0.63	0.82	0.79	0.70	0.75	0.74	0.69	0.71	0.70	-	-	-	-	0.70	0.78	-	-
Stride length [cm]	52.9	28.5	13.4	6.0	6.6	8.5	8.9	13.9	17.9	11.6	16.1	31.2	34.0	22.3	30.1	6.6	6.5	12.5	11.0
stance time [s]	1.65	0.98	0.46	0.86	1.11	0.33	0.43	1.37	0.86	1.09	0.78	-	-	-	-	0.54	0.64	-	-
swing time [s]	1.06	0.58	0.27	0.19	0.30	0.14	0.14	0.50	0.39	0.44	0.33	-	-	-	-	-	-	-	-
stride time [s]	2.71	1.56	0.73	1.05	1.41	0.47	0.57	1.89	1.25	1.54	1.11	-	-	-	-	0.77	0.82	-	-
speed [cm/s]	19.5	18.3	18.4	5.8	4.7	18.1	15.5	7.4	14.6	7.4	14.6	22.0	25.0	25.0	23.5	-	-	8.0	8.0
frequency [Hz]	0.37	0.64	1.37	0.95	0.71	2.12	1.74	0.53	0.80	0.65	0.90	0.71	0.74	1.12	0.78	1.30	1.22	0.64	0.73
Froude Number	0.74	1.20	2.57	0.56	0.34	3.92	2.76	0.40	1.17	0.50	1.33	1.58	1.88	2.86	1.87	1.13	0.98	0.52	0.59

**Extended Data 3: Extant animal data.**

Table (a): Experimental subjects analyzed. TL: total length; IGD: inter-girdle distance (gleno-acetabular distance). \*For comparison, data for the holotype specimen of *Orobates pabsti* measured using the digital reconstruction of the holotype specimen are provide<sup>18</sup>.

Table (b): Gait parameters and calculated Froude Numbers of different sprawling posture species. (a) Spectacled caiman (*Caiman crocodilus*). (b) Green iguana (*Iguana iguana*). (c) Blue-tongued skink (*Tiliqua scincoides*). (d) Mexican salamander (*Ambystoma mexicanum*). (e) Averaged data for salamander (*Pleurodeles waltl*)<sup>23</sup>. (f) Forelimb and (g) hindlimb of Leopard gecko (*Eublepharis macularius*)<sup>45</sup>. (h) Low speed sprawling posture, (i) high speed sprawling posture, (j) low speed high walk posture and (k) high speed high walk posture of alligator (*Alligator mississippiensis*)<sup>46</sup>. Savannah monitor lizards (*Varanus exanthematicus*)<sup>47</sup>. (l) lizard 1, (m) lizard 2, (n) lizard 3, and (o) lizard 4. (p) Forelimb and (q) hindlimb of Leopard gecko (*Eublepharis macularius*)<sup>48</sup>. (r) Male and (s) female Blue-tongued skink in a previous treadmill study (*Tiliqua scincoides*)<sup>37</sup>. Colors indicate the same source of information. The Froude number was calculated as  $Fr=h(f)^2g^{-1}$ , where h is the stride length, f is the gait frequency and g gravity (9.81 ms<sup>-2</sup>).

a	Orobates mass [kg]			% Orobates	OroBOT mass[kg]	% OroBOT	% differences
	Max	Min	Avg				
Head	0.213	0.213	0.213	5.35	0.389	6.29	0.93
Neck	0.260	0.113	0.187	4.68	0.232	3.75	-0.94
Front limb	0.273	0.182	0.228		0.359		0.0
x2	0.546	0.364	0.455	11.43	0.718	11.60	0.17
Trunk	2.749	1.369	2.059	51.72	3.224	52.09	0.37
Hind limb	0.447	0.255	0.351		0.541		0.0
x2	0.894	0.510	0.702	17.63	1.082	17.48	-0.15
Tail	0.549	0.182	0.366	9.18	0.544	8.79	-0.39
Totals	5.211	2.751	3.981	100.0	6.189	100.0	0.0

c	Orobates [cm]	x1.4 Head Orobates [cm]	x1.6 Scaled Orobates [cm]	x1.4 Head + x1.6 Scaled Orobates [cm]	% Orobates	OroBOT [cm]	% OroBOT	% differences
Neck	4.24	4.24	6.79	6.79	4.73	9.65	6.78	-2.05
Pectoral Girdle	7.96	7.96	12.73	12.73		13.05		-0.29
Spine	19.65	19.65	31.45	31.45		27.08		2.90
Pelvic Girdle	8.10	8.10	12.95	12.95		15.30		-1.72
Trunk	35.71	35.71	57.13	57.13	39.85	55.43	38.98	0.88
Tail	34.05	34.05	54.48	54.48	38.0	53.15	37.37	0.63
Total length	85.14	89.60	136.22	143.35	100.0	142.23	100.0	0.0
PectoralG Width	6.75	6.75	10.80	10.80	10.80			
Front Limb	18.67	18.67	29.87	29.87	31.47			
PelvicG Width	6.07	6.07	9.71	9.71	9.71			
Hind Limb	20.65	20.65	33.05	33.05	33.46			
IGD	27.30	43.68	43.68			43.68		
SVL	51.09	81.74	88.87			89.08		
CoM	12.36	19.77	19.77			19.80		

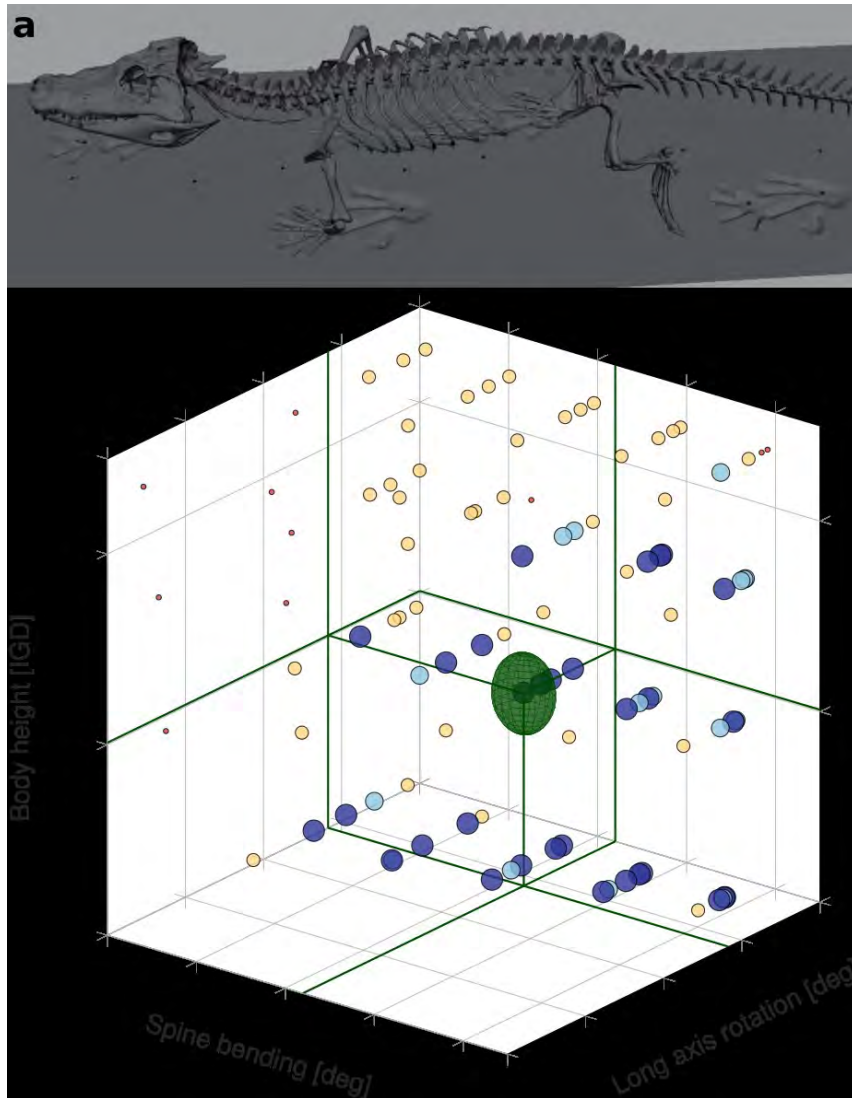
OroBOT Body part	Mass [g]
head	389.0
neck	232.0
neck mx64	142.0
pectoral girdle + 2x yaw mx64	736.0
2x pitch mx64	284.0
2x roll mx64	284.0
humerus	39.0
elbow mx64	142.0
antebrachium	48.0
wrist mx28	80.0
front foot	50.0
spine 1	259.0
spine 2	250.0
spine 3	220.0
pelvic girdle + 2x yaw mx64	765.0
2x pitch mx64	284.0
femur + roll mx64	201.0
knee mx64	142.0
crus	48.0
ankle mx28	80.0
hind foot	70.0
tail0	37.0
tail1	246.0
tail2	231.0
tailtip	30.0

Extended data 4: **Fossil/Robot mass distribution (Tables a and b) and dimensions (Table c).**

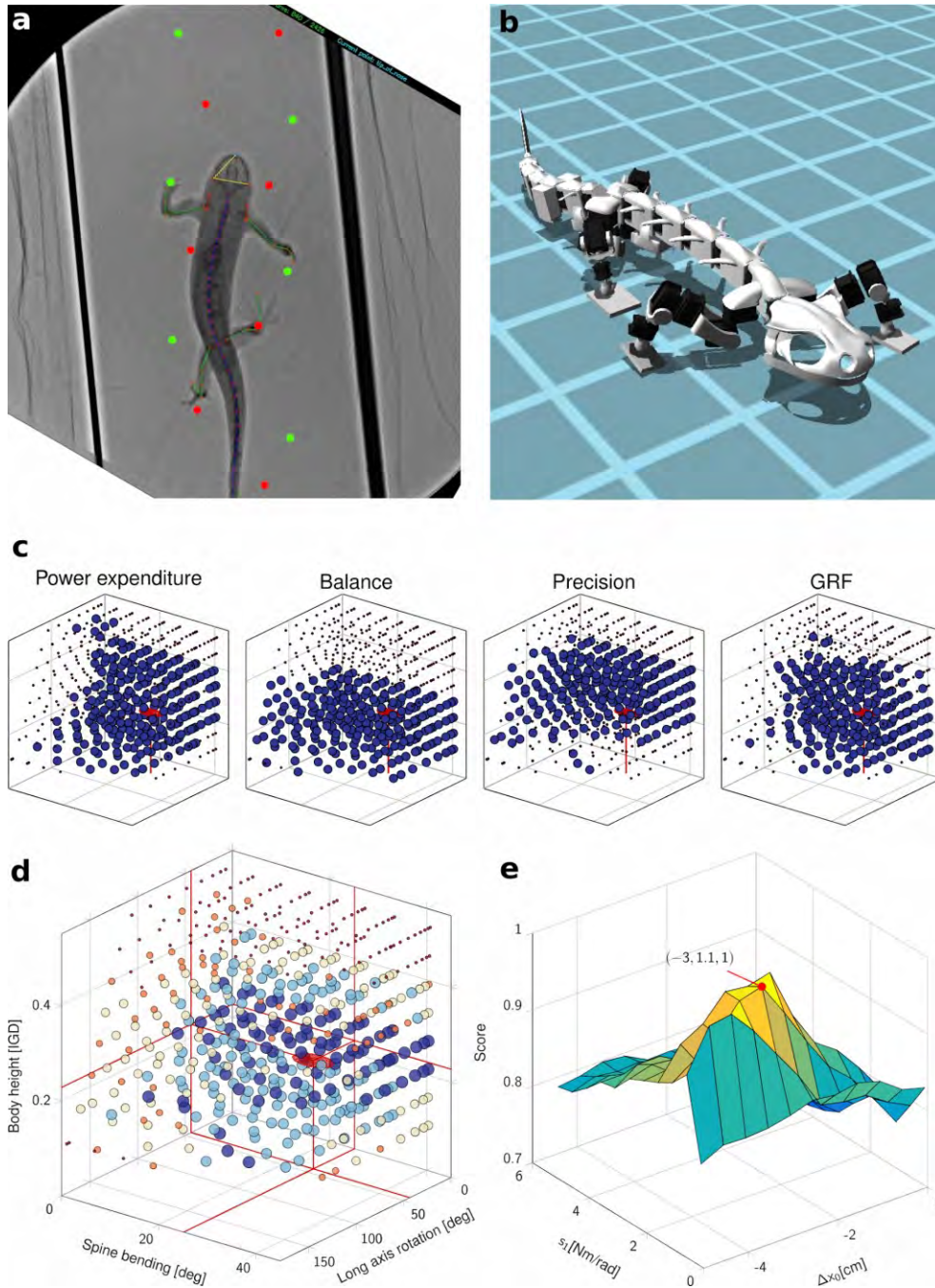
Table (a): Fossil/robot mass distribution. We used data for *Orobates*<sup>17</sup>. We averaged max and min plausible values of the mass of different body segments and calculate their ratios against the total body mass (also reported in Extended Data 1c). Same procedure was done for OroBOT. Differences between the mass ratios are calculated.

Table (b): OroBOT mass breakdown. Mass segments correspond to a 3D printed structural part with their associated servo motors. This is the case for neck, spine and tail segments. Similarly, the head segment contains also the mass of the robot's computer and other electronic peripherals (i.e power regulator, communication, Bluetooth and Wi-fi modules). In the case of the limbs, they are composed by individual servo motors, attached to each other by small 3D printed plastic light parts i.e. Humerus/Femur, aluminum parts i.e. Antebrachium/Crus, and their corresponding plastic feet. *Orobates* had a clear difference between front and hind limb mass. Which is noticeable also by the cross sectional areas of the Humerus/Femur. This difference was hard to replicate with the materials and dimensions used in the robotic reconstruction (i.e. similar fabrication and mass for front and hind limbs). Consequently, the mass of the first and second shoulder servo motors in the forelimbs were associated with the front girdle mass, and considered as part of the trunk. In the case of the hindlimbs, only the first shoulder servo motor was considered part of the hind girdle, hence part of the trunk as well.

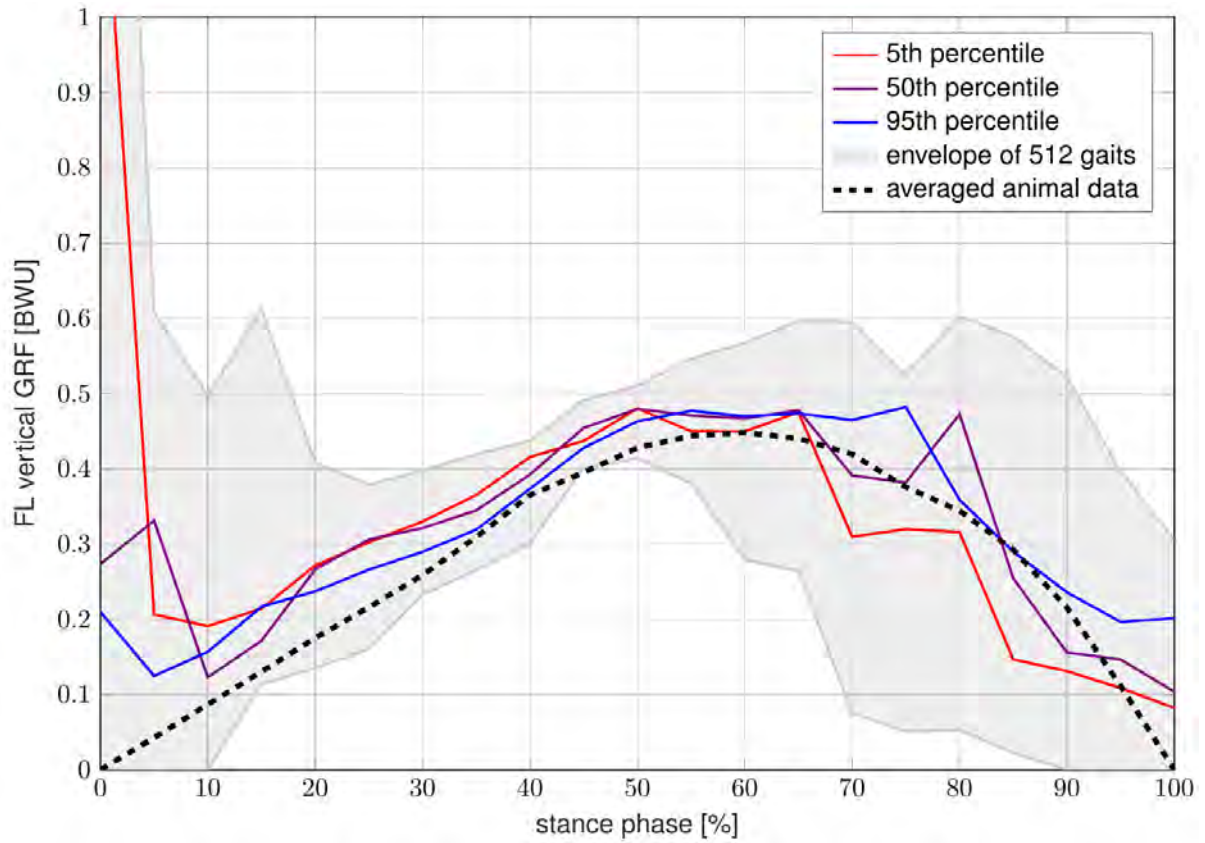
Table (c): Length comparison between different body segments in *Orobates* and OroBOT. Organized by columns: (i) *Orobates* dimensions. (ii) *Orobates* with an initial head scale of 1.4:1 (Extended Data 1a). (iii) *Orobates* with a body scale of 1.6:1 (no head additional scaling) (Extended Data 1b). (iv) Final desired lengths of *Orobates* head and body scaled. (v) Segments to body length ratios (Extended Data 1c). (vi) Final OroBOT dimensions. (vii) OroBOT segments to body length ratios (Extended Data 1c). (viii) Mass distribution ratio differences between scaled *Orobates* and OroBOT. Data for *Orobates* taken from<sup>17</sup>. Trunk consisted of pectoral girdle, spine segments and pelvic girdle. Girdles and spine segments are depicted in light green. CoM of OroBOT was calculated using the CAD files in Autodesk Inventor® 2017 and confirmed by manual measurements.



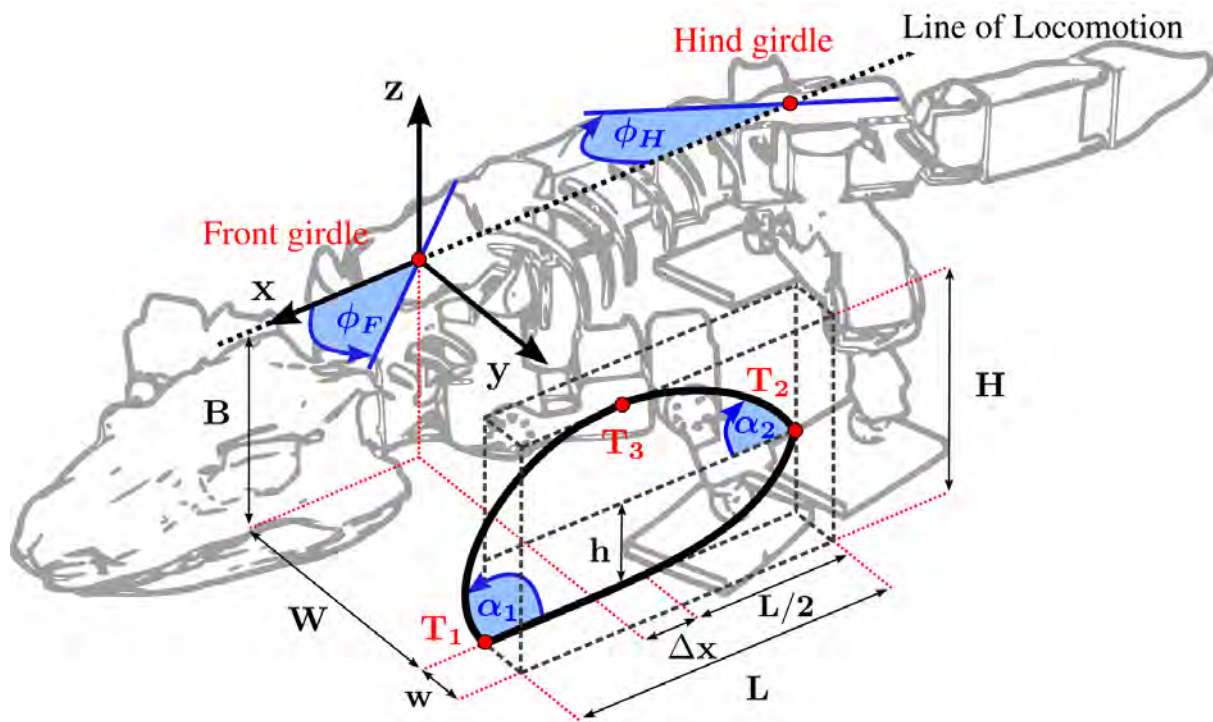
Extended Data 5: **Kinematic simulation workflow validation using caiman.** (a): Maya screenshot of caiman digital marionette walking within digitized caiman trackways (see Methods). (b):  $n=100$  hindlimb parameter combinations of body height, spine bending, and LAR were tested (in the same way as described for *Orobates* kinematic simulation). Scores for each combination were coded by size of the dots (largest dots assigned to perfect plausibility) and colour (dark blue assigned to perfect plausibility). Green ellipsoid depicts mean measured kinematics of caiman hindlimb from the x-ray motion analysis  $\pm$  standard deviation ( $n=8$ ; green lines project the means of  $x$ ,  $y$ ,  $z$  onto the plane to improve readability). Note that body height less than 0.4 resulted in the body moving through the ground and spine bending over  $60^\circ$  resulted in bone collisions within the spine. Actual caiman kinematics (green ellipsoid) are nested within the domain identified as anatomically plausible (dark blue points), demonstrating the validity of the kinematic simulation workflow.



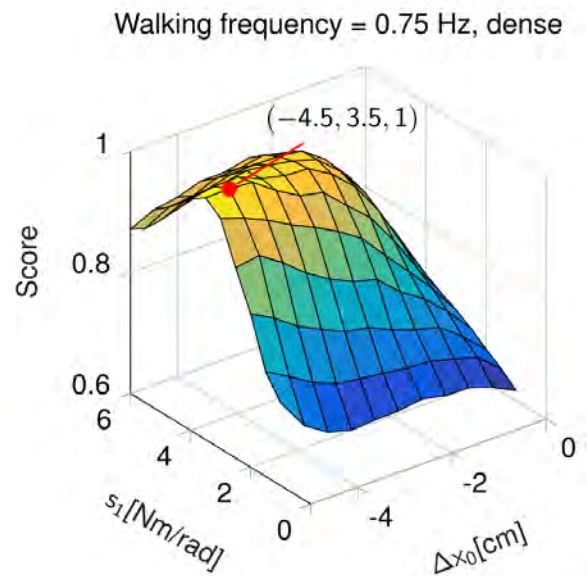
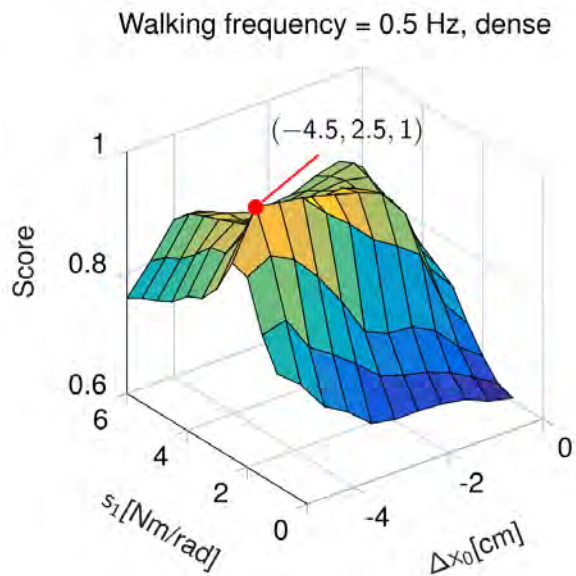
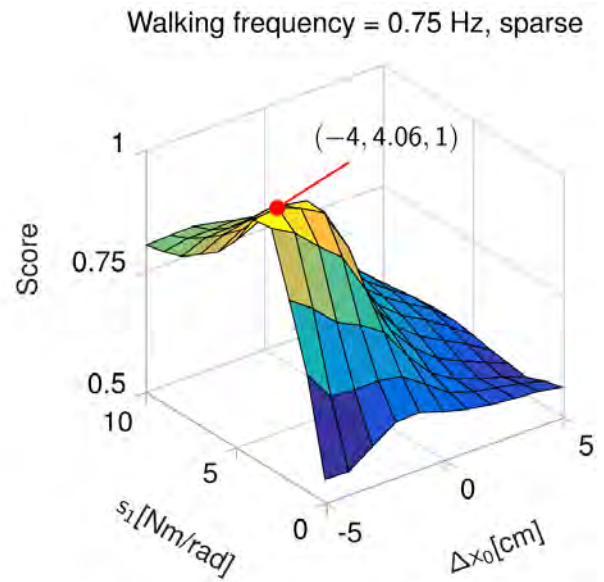
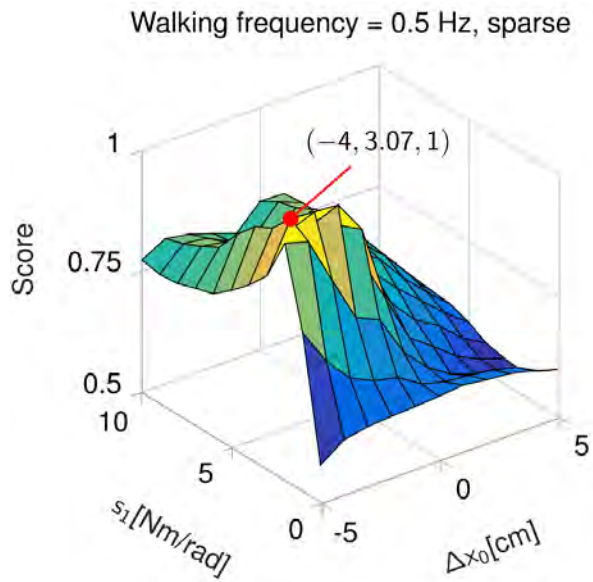
Extended Data 6: **Validation of the dynamic simulation workflow with *Pleurodeles*/Pleurobot.** **(a)** Construction of *Pleurodeles* “trackways” from a top-view x-ray video. **(b)** Pleurobot - a salamander-like robot used to reconstruct the salamander *Pleurodeles* gait<sup>23</sup>. Details of selection of gait parameters as in Extended Data 8. **(c)** Individual metric scores with the binary threshold set to 50 (50th percentile). With such exclusion, all the metrics predict a region containing the *Pleurodeles* gait (in red)  $n=2$  for body height ( $0.23 \pm 0.01$  IGD),  $n=21$  for spine bending ( $(50.29 \pm 7.96)/2$  deg) and LAR ( $43.46 \pm 9.55$  deg) (Supplementary Data 15). Note in particular the low body height (around 0.2) compared to caiman (around 0.5, Extended Data 5). **(d)** Summed scores of the 4 dynamic metrics (power expenditure, balance, precision and GRF) in the hindlimb space with the binary threshold set to 50. **(e)** Exploration of Pleurobot’s optimal foot stiffness and trajectory offset values (as in Extended Data 9) for the walking frequency of 0.25Hz (found by dynamic similarity analysis as in<sup>23</sup>).



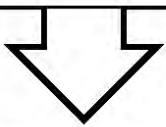
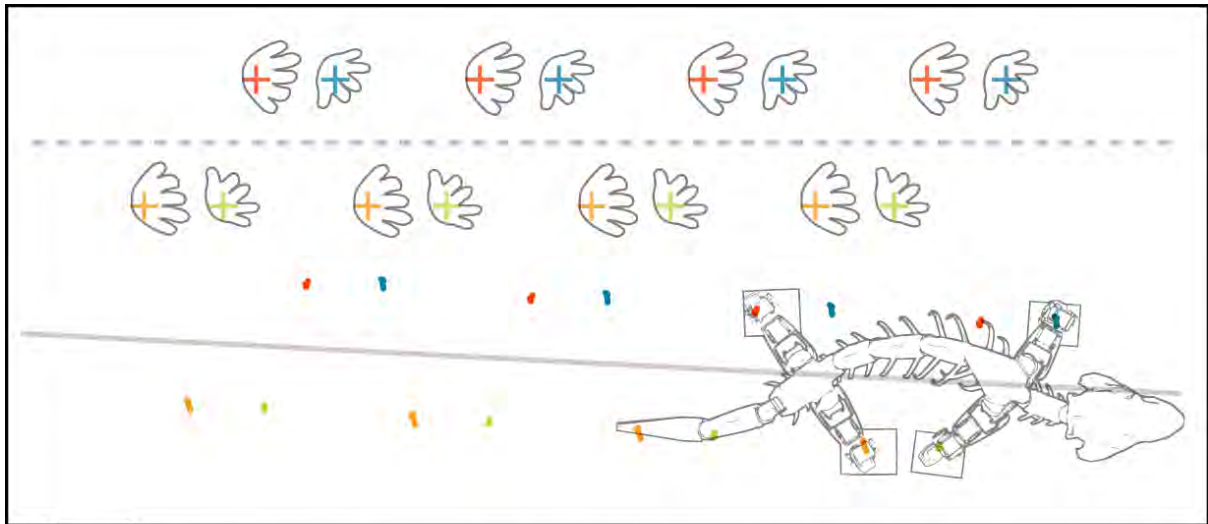
Extended Data 7: **Vertical ground reaction force profile of simulated OroBOT's forelimbs.** The force profiles of gaits that scored low (5th percentile score), average (50th percentile) and high (95th percentile) in the GRF metric are shown and compared to the averaged force profile observed in the extant species (n=38 trials). The gray area shows the area within which the force profiles of all n=512 simulated gaits are located. The high force values of some gaits at the beginning of a stance phase are the result of foot-ground impacts while transitioning from swing to stance phase.



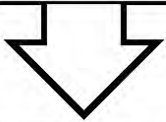
Extended Data 8: **OroBOT's reference frame and kinematic gait parameters.** The foot trajectory, composed of a stance phase ( $\mathbb{T}_1 \rightarrow \mathbb{T}_2$ ) and a swing phase ( $\mathbb{T}_2 \rightarrow \mathbb{T}_3 \rightarrow \mathbb{T}_1$ ), was defined in the reference frame of the corresponding girdle. The spine motion was determined by rotation of the girdles about their vertical axis.



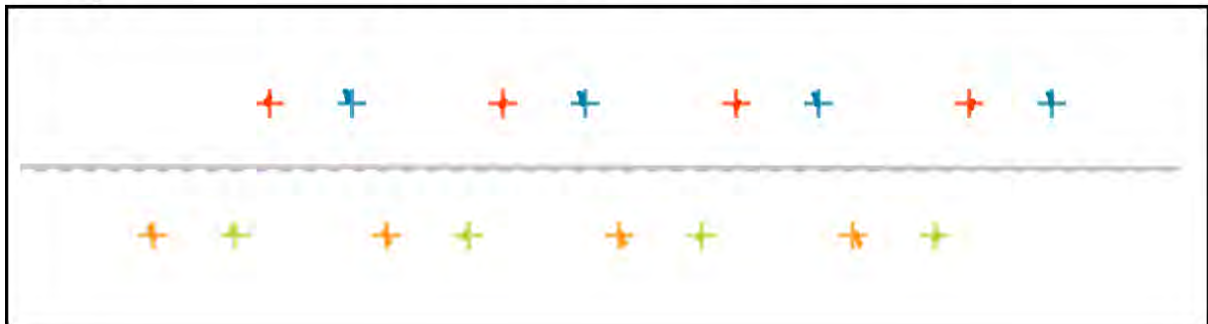
Extended Data 9: **Exploration of the optimal foot stiffness and trajectory offset values.** The exploration was done in two steps: on the coarse grid of foot parameters to get a region of the optimum (top) and on the dense grid to refine the optimum (down). The process was repeated for two frequencies: 0.5Hz (left) and 0.75Hz (right).



Align the centerlines (rotation and translation)



Minimize the distance between the targets and robot footsteps (translation)



Extended Data 10: **Computation of the precision metric** (Supplementary Information 1). (**Top**) The idealized trackways (Extended Data 1k) and the robot footsteps extracted from Webots simulation were not necessarily aligned in the world reference frame, since the robot did not use path-following strategies. (**Middle**) The trackways and the footsteps were approximately aligned by matching their centrelines via translation and rotation. (**Bottom**) A precise alignment was done by translation, whose amount was determined through an optimization that minimized distances between the corresponding footsteps. The remaining distances were summed and used as a measure of precision.